Astron. Astrophys. 358, 793–811 (2000)

ASTRONOMY AND ASTROPHYSICS

Microlensing of multiply–imaged compact radio sources

Evidence for compact halo objects in the disk galaxy of B1600+434

L.V.E. Koopmans[1] **and A.G. de Bruyn**[2,1]

[1] Kapteyn Astronomical Institute, P.O. Box 800, 9700 AV Groningen, The Netherlands
[2] NFRA, P.O. Box 2, 7990 AA Dwingeloo, The Netherlands

Received 15 October 1999 / Accepted 11 April 2000

Abstract. We present the first unambiguous case of external variability of a radio gravitational lens, CLASS B1600+434. The *Very Large Array* (VLA) 8.5–GHz difference light curve of the lensed images, taking the proper time-delay into account, shows the presence of external variability with 14.6–σ confidence.

We investigate two plausible causes of this external variability: scattering by the ionized component of the Galactic interstellar medium and microlensing by massive compact objects in the bulge/disk and halo of the lens galaxy. Based on the tight relation between the modulation-index (fractional rms variability) and variability time scale *and* the quantitative difference between the light curves of both lensed images, we conclude that the observed short-term variability characteristics of the lensed images are incompatible with scintillation in our Galaxy. This conclusion is strongly supported by multi–frequency *Westerbork Synthesis Radio Telescope* (WSRT) observations at 1.4 and 5 GHz, which are in disagreement with predictions based on the scintillation hypothesis. Several arguments against scintillation might need to be reevaluated if evidence is found for significant scatter-broadening of lensed image B seen through the lens galaxy. However, the frequency-dependence and time scale of variability from image A are not affected by this and remain strong arguments against scintillation.

On the other hand, a single superluminal jet-component in the source, having an apparent velocity $9 \lesssim (v_{\rm app}/c) \lesssim 26$, a radius of 2–5 μas and containing 5–11% of the observed 8.5–GHz source flux density, can reproduce the observed modulation-indices and variability time scale at 8.5 GHz, when it is microlensed by compact objects in the lens galaxy. It also reproduces the frequency-dependence of the modulation-indices, determined from the independent WSRT 1.4 and 5–GHz observations. The difference between the modulation-indices of the lensed images (i.e. 2.8% and 1.6% at 8.5 GHz in 1998 for images A and B, respectively), if not affected by scatter-broadening of image B by the ionized ISM of the lens galaxy, can be explained through a different mass-function for the compact objects in the bulge/disk and halo of the lens galaxy. Comparing the observations with microlensing simulations, we place a tentative lower limit of $\gtrsim$0.5 $M_\odot$ on the average mass of compact objects in the halo line-of-sight. The above-mentioned set of mass-function and source parameters is consistent, although not unique, and should only be regarded as indicative.

The only conclusion fully consistent with the data gathered thus far is that we have indeed detected *radio microlensing*. The far reaching consequence of this statement is that a significant fraction of the mass in the dark–matter halo at $\sim$6 kpc (h=0.65) above the lens–galaxy disk in B1600+434 consists of massive compact objects.

Key words: cosmology: dark matter – cosmology: gravitational lensing – galaxies: halos – galaxies: ISM – galaxies: spiral – galaxies: structure

1. Introduction

Gravitationally lensed compact radio sources have many astrophysical and cosmological applications. The foremost being the determination of a time-delay between the individual lensed images in order to constrain the Hubble parameter (e.g. Refsdal 1964). Considerable progress has been made during the last few years in measuring time-delays, both through optical and radio observations (e.g Kundić et al. 1997; Schechter et al. 1997; Lovell et al. 1998; Biggs et al. 1999; Fassnacht et al. 1999; Koopmans et al. 2000). They also allow a detailed study of the mass distribution of the lens galaxy and sometimes the background source, through a large magnification by the lensing potential. Absorption lines in the spectrum of the background source allow the study of the ISM in the lens galaxy and the HI distribution along the lines of sight to the source.

Temporal changes in the brightnesses or spectra of the lensed images also allow the study of uncorrelated external variability. The most important sources of external variability are scintillation at radio wavelengths and microlensing in all wavelength bands. Differencing the image light curves, taking the proper time delay into account, removes intrinsic source variability and leaves only uncorrelated external variability. These difference light curves thus provide valuable information on the compact objects in the lens galaxy and/or on the intervening ionized

Send offprint requests to: L.V.E. Koopmans
Correspondence to: leon@astro.rug.nl

medium (e.g. Lehár et al. 1992; Haarsma et al. 1997; Schmidt & Wambsganss 1998).

The study of the ionized component of the Galactic interstellar medium (ISM) through scattering of radio emission from pulsars has had a long tradition (e.g. Rickett 1977, 1990). Scattering by the ionized ISM can explain long-term variability at meter wavelengths (e.g. Condon et al. 1979), as well as large-amplitude variability in very compact extra-galactic radio sources (e.g. Rickett, Coles & Bourgois 1984). Low-amplitude variability at shorter wavelengths (about 10 cm), called 'flickering', has been observed by Heeschen (1982, 1984) and is probably associated with refractive interstellar scattering of an extended source (e.g. Rickett et al. 1984). Strong intra-day variability of very compact radio sources might result from refractive interstellar scattering as well (e.g. Wagner & Witzel 1995). A power-law model of the plasma-density power spectrum (e.g. Rickett 1977, 1990), combined with some distribution of this plasma in our galaxy (e.g. Taylor & Cordes 1993 [TC93]) is able to explain most of the observed dispersion measures and variability in pulsars at low frequencies, as well as the variability of extra-galactic radio sources at both low and high frequencies. However, especially for compact flat-spectrum radio sources it remains exceedingly difficult to separate intrinsic variability from scintillation by the Galactic ionized ISM.

Gravitationally lensed (i.e. multiply-imaged) flat-spectrum compact radio sources could offer a solution to this problem. As mentioned previously, these systems provide two or more lines-of-sight through the Galactic ionized ISM. For typical image separations of a few arcseconds, one is looking through parts of the Galactic ionized ISM separated by a few hundred AU. One can expect the scattering of radio waves to be independent for the different lines-of-sight. Differencing the image light curves, after a correction for the appropriate time delay and flux-density ratio, produces a difference light curve that only shows uncorrelated external variability. This difference light curve can be studied to obtain information on the Galactic ionized ISM independent from intrinsic source variability.

However, uncorrelated external variability of the lensed images might also originate from microlensing in the lens galaxy (e.g. Chang & Refsdal 1979). This offers the additional opportunity to study the properties of compact objects in the lens galaxy, if microlensing variability dominates or can be separated from scintillation. Optical microlensing in the lens galaxy of Q2237+0305 has unambiguously been shown (e.g. Irwin et al. 1989; Corrigan et al. 1991; Ostensen et al. 1996; Lewis et al. 1998; Woźniak et al. 2000). In the radio, several suggestions of microlensing variability have been made (e.g. Stickel et al. 1988; Quirrenbach et al. 1989; Schramm et al. 1993; Romero et al. 1995; Chu et al. 1996; Wagner et al. 1996; Lewis & Williams 1997; Takalo et al. 1998; Quirrenbach et al. 1998; Kraus et al. 1999; Watson et al. 1999). In none of these cases, however, has one really been able to convincingly distinguish between intrinsic and external variability. Claims of external variability in singly-imaged radio sources through microlensing should therefore be regarded with some caution.

In this paper, we report the first unambiguous case of external variability of a radio gravitational lens, CLASS B1600+434 (Jackson et al. 1995; Jaunsen & Hjorth 1997; Koopmans, de Bruyn & Jackson 1998 [KBJ98]; Koopmans et al. 2000 [KBXF00]). The system consists of two compact flat-spectrum radio images, separated by 1.4 arcsec. The background source, at a redshift of z=1.59, is lensed by an edge-on disk galaxy at a redshift of z=0.41 (Fassnacht & Cohen 1998). A time delay of 47^{+12}_{-9} days (95% statistical confidence) was recently found (KBXF00).

What is furthermore of interest is that this system offers two distinct lines-of-sight through the lens galaxy. Image A passes mainly through the dark-matter halo around the edge–on lens galaxy, whereas image B passes predominantly through its disk and bulge (Koopmans et al. 1998; Maller et al. 2000; CASTLE Survey, Munoz et al. 1999). This makes image A especially sensitive to microlensing by massive compact objects in the halo and image B to microlensing by stars in the disk and bulge. This might even offer an opportunity to study compact objects in the dark–matter halo around the lens galaxy of B1600+434.

The outline of the paper is as follows. In Sect. 2, we present the VLA 8.5–GHz data from KBXF00 in a different way, unambiguously showing the presence of external variability. We also present additional WSRT 1.4 and 5–GHz monitoring data of B1600+434. In Sect. 3, we investigate whether Galactic scintillation can explain the fractional rms variabilities (modulation-indices) and time scales of the short-term variability seen in the VLA 8.5–GHz light curves. Similarly, in Sects. 4 and 5 the possibility of microlensing by compact objects in the lens galaxy is studied. In Sect. 6, we present microlensing simulations of a more complex jet structure and compare the results to B1600+434. In Sect. 7, we discuss a critical test (i.e. the frequency-dependence of the modulation-index) to discriminate between scintillation and microlensing *and* compare predictions from the VLA 8.5–GHz light curves with the independent multi-frequency WSRT data. In Sect. 8 our results and conclusions are summarized.

2. Short-term variability in B1600+434–A & B

B1600+434 is a compact ($\lesssim$1 mas at 8.5 GHz; KBXF00) radio source, which has varied strongly at 8.5 GHz since its discovery in 1994 (Jackson et al. 1995). Its flux density decreased from 58 (48) mJy in March 1994 to only 29 (24) mJy in August 1995 for image A (B) (KBJ98). From February to October 1998, another decrease from 27 (24) to 23 (19) mJy was found (KBXF00). In June 1999, the flux densities appear to have stabilized to 23 (17) mJy. Strong variability was also observed at 5 GHz, where a total flux density was measured of 34–37 mJy in 1987 (GB87; Becker, White and Edwards 1991). Observations in March 1995 gave 45 (37) mJy for image A (B) (KBJ98), whereas in June 1999 this had reduced to only 23 (18) mJy. At 1.4 GHz, the integrated WSRT flux density of B1600+434 has decreased from 60–65 mJy in April–July 1996 (KBJ98) to about 50 mJy in June 1999.

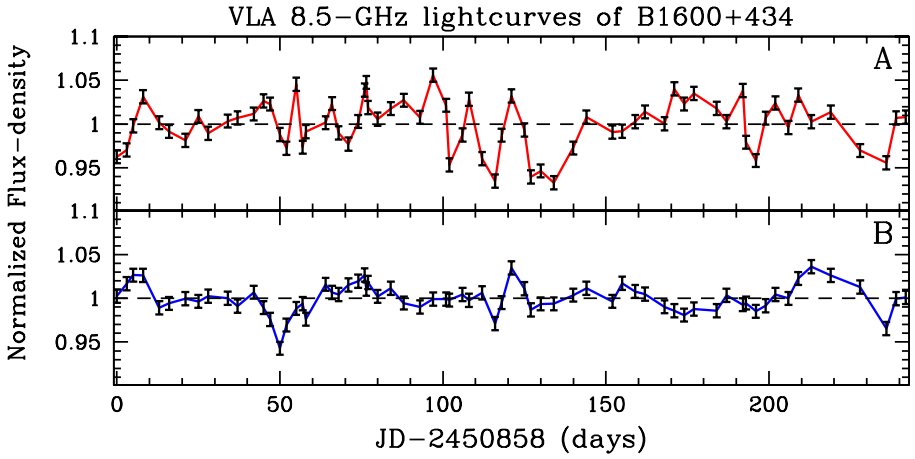

Fig. 1. The normalized light curves of B1600+434 A (upper) and B (lower), corrected for a long-term gradient (Sect. 2). The error on each light-curve epoch is 0.7 to 0.8% (1–σ). Day 0 corresponds to 1998 Febr. 13

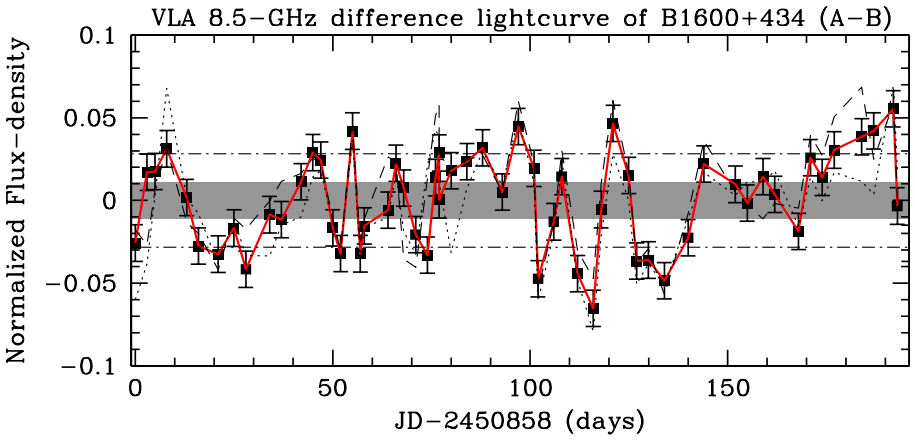

Fig. 2. The normalized difference light curve between the two lensed images, corrected for both the time-delay and flux density ratio (Sect. 2.1). The shaded region indicates the expected 1–σ (1.1%) region if all variability were due to measurement errors. The dashed–dotted lines indicate the observed modulation-index of 2.8%. The dotted and dashed curves indicate the normalized difference curves for a time delay of 41 and 52 days, respectively. Obviously most variations can not be explained by any reasonable error in the time delay. There seems to be no evidence of any change in the typical time scale of variability over 6 months. Day 0 corresponds to 1998 Febr. 13.

Because of this strong variability, B1600+434 was observed from February to October 1998 with the VLA at 8.5 GHz, in order to measure a time delay between the two lensed images. In KBXF00, the VLA 8.5–GHz light curves of the two lensed images were presented, showing short-term variability, as well as a long-term decrease in the flux density of both lensed images, which we assume to be intrinsic source variability similar to that seen in, for example, Q0957+561, in which no apparent external variability has been found thus far (e.g. Lehár et al. 1992; Haarsma et al. 1997).

In Fig. 1, the normalized VLA 8.5–GHz light curves of both lensed images are shown. The curves were created by dividing the light curves by linear fits (KBXF00). The resulting curves show the fractional variability on short time scales (i.e. shorter than the observing period of about 8 months) with respect to the running mean. The 1–σ error for each point on the light–curve is 0.7 to 0.8% (KBXF00). We omitted the six strongest outliers from both plots, which show clear systematic problems with the data or calibration (KBXF00). The resulting normalized light curves have modulation indices (i.e. fractional rms variabilities) of 2.8% and 1.6% for images A and B, respectively. We use these values throughout this paper. Lensed images A and B have modulation-indices significantly larger than expected on the basis of the measurement errors only, indicating the clear presence of short-term variability, either intrinsic or external. The structure functions (e.g. Simonetti, Cordes, & Heeschen 1985) of the normalized light curves are shown in Fig. 6 (Sect. 3.2).

2.1. Intrinsic or external variability?

To show that most of the short-term variability is of external origin, the linearly-interpolated light curve of image B was subtracted from the light curve of image A, taking a flux-density ratio of 1.212 and a time delay of 47 days into account (KBXF00). The time delay was determined with the minimum-dispersion method from Pelt et al. (1996). Hence, the modulation-index of the normalized difference light curve, shown in Fig. 2, is by definition a lower limit. This is illustrated by the dotted and dashed lines, which show the normalized difference light curves for a time delay of 41 d and 52 d (i.e. the 68% confidence region), respectively. Both curves have larger modulation-indices, as should be expected.

The normalized difference light curve has a modulation-index of 2.8%. This is significantly larger than the modulation-index of 1.0–1.1% (i.e. the shaded region in Fig. 2), which one would expect on the basis of the measurement errors only. Most of the short-term variability present in the light–curves must therefore be of external origin. A χ^2–value of 377 was deter-

mined from the 58 points composing the difference light curve. This is inconsistent with a flat difference light curve at the 14.6–σ confidence level.

If the short–term variability of the two lensed images is uncorrelated, the expected modulation-index in the normalized difference curve should be $\sqrt{(2.8^2+1.6^2)}\approx$3.2%, which is slightly larger than the observed value of 2.8%. It remains hard to assess whether individual features in the light curves might be of intrinsic origin. In this paper we will therefore assume that *all* short–term variability in both lensed images is of external origin.

2.2. WSRT 1.4 & 5–GHz monitoring

Before proceeding with the analysis of the VLA 8.5–GHz light curves, we first present multi-frequency WSRT total-flux-density data of B1600+434 obtained in 1998/9 at 1.4 and 5 GHz. This data will play an essential role in distinguishing between the different physical mechanisms causing the external variability observed in the VLA 8.5–GHz lensed-image light curves, as we will see in Sect. 7.

Starting in August 1998 the WSRT was outfitted with a series of new multi-frequency front-ends (MFFE's) that can operate at frequencies from 0.3 to 8.5 GHz. When the WSRT observations of B1600+434 were begun in August 1998 only 6 front-ends were available at 1.4 GHz. The available number of telescopes with MFFE's increased at a rate of about 1 per month until the full array was outfitted in February 1999. Towards the end of 1998 the monitoring was extended to include 5 GHz. In the spring of 1999 we also included 8.5–GHz observations. However, the analysis of the 8.5–GHz data is still encountering some problems and we therefore do not report on the results of the 8.5–GHz observations here.

Each run consisted of two sets of observations (at up to 3 frequencies) on B1600+434 and the nearby reference source B1558+439. The latter is a strong steep spectrum double radio source (0.8–arcsec size) about 40 arcmin north-east of B1600+434. In each run we also observed two primary calibration sources (3C286, 3C343 and CTD93). Although we changed the details of the observing sequence during the year the basic structure did not change.

The resolution of the WSRT is about 12×18 arcsec (1.4 GHz) and 3.5×5 arcsec (5 GHz). B1600+434 is therefore always unresolved at 1.4 GHz. At 5 GHz the source, however, shows slight hour-angle dependent resolution effects [the WSRT is an east-west synthesis array, hence the instantaneous synthesized response is a fan beam rotating clockwise on the sky]. Because the observations were scheduled at random hour angles the resolution effect is therefore variable from session to session. We minimized the magnitude of this effect by determining the flux density using only baselines up to 1300 meter; the residual effect on the flux density is below the thermal noise error.

The amplitude and flux calibration was performed in NEWSTAR using standard procedures starting with a selfcalibration on the primary reference source. The complex telescope gains were then transferred to the target and reference source. The flux densities of B1600+434 and B1558+439 were then determined using a uv-plane fitting algorithm in the program NMODEL. Selfcal phase solutions on the reference source B1558+439 usually showed only very slight decorrelation effects due to slow instrumental/atmospheric phase-drifts. Because these would be very similar for B1600+434 and the reference source we decided not to apply a phase selfcal solution.

The flux density of the reference source B1558+439 was found to show a scatter of about 1–2% around 700 mJy at 1.4 GHz and about 1.0% around 204 mJy at 5 GHz. This scatter is still larger than the noise error on the flux density. We believe these can be attributed to small changes in atmospheric opacity and small instrumental gain drifts (e.g. due to pointing). Normalizing the amplitudes of B1600+434 by those of the reference source should eliminate them. We therefore expect that the final errors on the flux density of B1600+434 are determined by the thermal noise only. Still, to be on the safe side we adopted as a final error on the flux density of B1600+434 the quadrature sum of the thermal noise level and a 1% scale error. This amounts to a typical error of 1.0% and 1.3% at 1.4 and 5 GHz, respectively.

In Fig. 3, we have shown the calibrated WSRT 1.4–GHz (L–band) and 5–GHz (C–band) light curves, together with the total-flux-density VLA 8.5–GHz (X–band) light curve (KBXF00). We note the following properties: (i) All light curves are dominated by systematic trends with decreasing intensity at 8.5 and 1.4 GHz, but increasing at 5 GHz. We believe these changes to be due to intrinsic variations. (ii) If the VLA 8.5–GHz and WSRT 5–GHz long-term intrinsic flux-density variations are correlated, there has been a clear trend-break in the gradient of the light curves around day 300 (Fig. 3). The WSRT 1.4–GHz light curve still shows a similar gradient as the VLA 8.5–GHz light curves in 1998, hence there appears to be a time-lag of at least 200 days between long-term intrinsic source variability at 8.5 and 1.4 GHz. This trend-break is supported by the first results from the 1999 VLA campaign (Koopmans et al. in prep.). (iii) At those epochs where the light curves overlap, the higher-frequency light curves show a larger short-term modulation-index around the long-term linear gradient.

An important statistical property of the light curves is their modulation-index on short time scales (i.e. time scales shorter than the length of the light curves), as function of frequency. To calculate the modulation-indices, we divide the light curves through a linear fit (see Sect. 2) in order to remove most of the presumably intrinsic source variability. The results are normalized light curves, similar to the normalized VLA 8.5–GHz light curves shown in Fig. 1. We only calculate the 1.4 and 5–GHz modulation indices ($m_{\rm part}$) for those epochs, where we have both 1.4 and 5–GHz WSRT flux-density measurements. The normalized light curves of these epochs are shown in Fig. 4. The resulting modulation-indices are listed in Table 1. Because the modulation-index at 1.4 GHz is very close to the estimated flux-density error, we regard it as an upper limit.

The total flux-density modulation-indices in Table 1 are a combination of the individual modulation-indices of images A and B. If we assume that the ratio of modulation-indices are

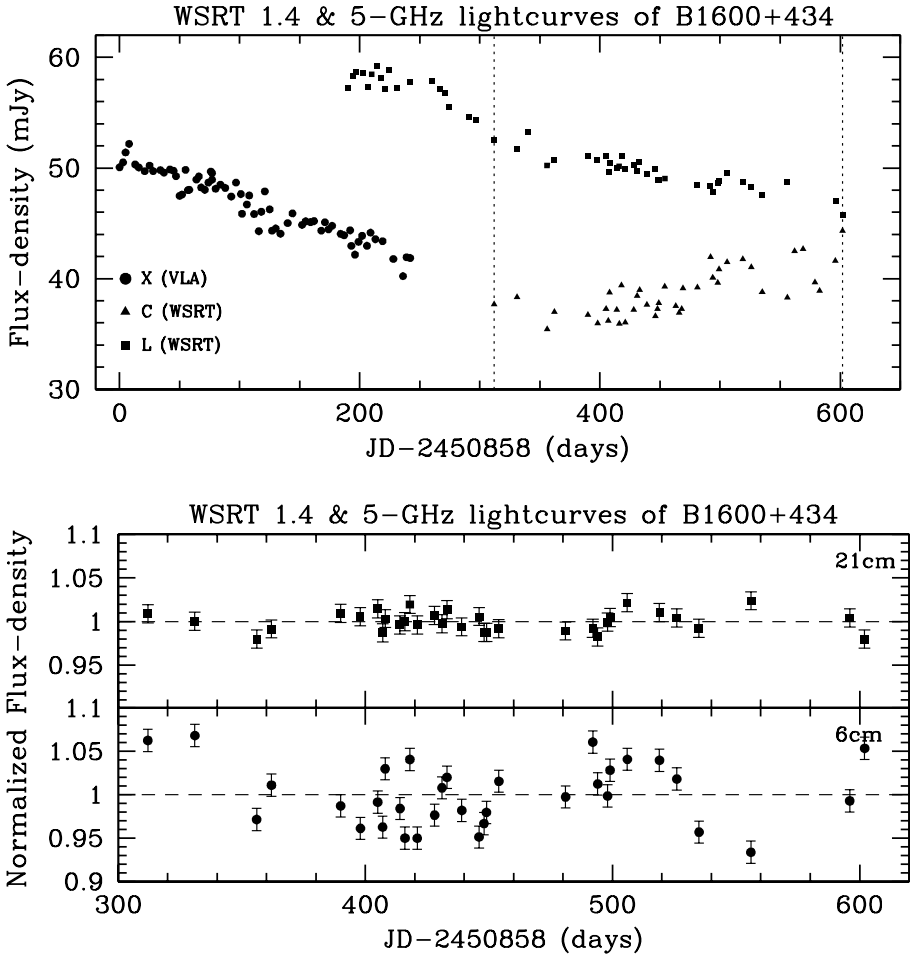

Fig. 3. The integrated flux-density light curves of B1600+434 (sum of lensed images A and B) in X–band (VLA 8.5 GHZ), C–band (WSRT 5 GHz) and L–band (WSRT 1.4 GHz). The two vertical dashed lines indicate the time-span, where the WSRT 1.4 and 5–GHz observations overlap. Day 0 corresponds to 1998 Febr. 13

Fig. 4. The normalized WSRT 1.4 and 5–GHz flux-density light curves of B1600+434. Only those epochs of the WSRT light curves are shown that have both a 1.4 and 5–GHz measurement (Fig. 3). The light curves were created similar to the VLA 8.5–GHz light curves shown in Fig. 1. One notices a clear increase in the modulation-index from 21 to 6 cm by a factor $\sim$3

Table 1. The short-term total flux-density modulation-indices of B1600+434, as function of frequency

ν (GHz)	$m_{\rm part}$ (%)	Epoch (days)	Instr.
1.4	$\leq$1.2	312–602	WSRT
5.0	3.7	312–602	WSRT

equal to those at 8.5 GHz (i.e. $(m_{\rm A}/m_{\rm B})_\lambda \approx 2.8/1.6=1.75$) for each wavelength, we only make a slight error ($\lesssim$15%) compared to the assumption that image B does not vary at all on short time scales. Because we will *only* use modulation-index ratios (see Sect. 7), which are independent from these assumptions in first order, this is of negligible importance.

2.3. Possible origins of the external variability

What can be the origin of the external variability seen in the VLA 8.5–GHZ light curves, why does the modulation-index differ between the two image light curves and what causes the short-term variability in the WSRT 1.4 and 5–GHz light curves? Below we have listed different physical mechanisms which can introduce external variability in the flux density of compact radio sources:

1. Scintillation
   - Weak scattering (Sect. 3.1)
   - Refractive scattering (Sect. 3.2)
   - Diffractive scattering (Sect. 3.3)
2. Microlensing (Sect. 4–5)

In the next three sections, we will investigate in detail whether one or more of these can explain the external variability seen in the VLA 8.5–GHz light curves of B1600+434–A & B. In Sect. 7, we will combine the conclusions from Sect. 3–5 with the results from the WSRT 1.4 and 5–GHz observations to further constrain the scintillation and microlensing hypotheses.

3. Scintillation

Even though the difference in modulation-index between images A and B seems to require a considerable change in the properties of the Galactic ionized ISM over an angular scale of 1.4 arcsec (Sect. 3.2), we still proceed to investigate whether the short-term variability, superposed on the gradual and presumably intrinsic long-term decrease of the flux density of the lensed images, can be the result of scintillation. We will follow the prescription of Narayan (1992) and its numerical implementation by Walker (1998; [W98]) for the Galactic ionized ISM model from TC93. This assumes that the inhomogeneities of

the ionized ISM can be described by a Kolmogorov power-law spectrum (e.g. Rickett 1977; Rickett 1990) and that the ionized ISM model from TC93 is approximately valid. Support for the approximate validity of the TC93 model in the direction to B1600+434 is given by the dispersion and scattering measures of nearby pulsars, showing no apparent deviations from this model. Also, no evidence is found in the low-frequency (327–MHz) WENSS catalogue (e.g. Rengelink et al. 1997) for diffuse HII emission or SN remnants that could introduce small-scale perturbations in the Galactic ionized ISM.

Depending on the line-of-sight through the galaxy and the observing frequency, the scattering of radio waves, expressed in the scattering strength ξ=$r_{\rm F}/r_{\rm diff}$, can be strong (ξ>1) or weak (ξ<1), where $r_{\rm F}$ is the Fresnel scale and $r_{\rm diff}$ is the diffractive scale (e.g. Narayan 1992). The transition between these two regimes occurs near a transition frequency (ν_0). For B1600+434 at a Galactic latitude of b=+48.6°, we find ν_0=4.2 GHz (W98). At the observing frequency of 8.5 GHz, scattering should therefore be in the weak regime ($\xi\sim$0.3). The transverse velocity of the ISM with respect to the line-of-sight to B1600+434 is determined by projecting the velocity vector of the earth's motion on the sky as function of time. We find a transverse velocity (v) between 20 and 40 km s^{-1}. We will therefore adopt an average value of v=30 km s^{-1} throughout this paper. For lack of better knowledge, we assume any intrinsic transverse motion of the scattering medium to be zero.

3.1. Weak scattering

The modulation-index of a point source in the weak scattering regime is (Narayan 1992)

$$m_{\rm p} = \left(\frac{\nu_0}{\nu}\right)^{17/12}. \quad (1)$$

In the simplest case that B1600+434 is a point source smaller than the Fresnel scale of 3.9 μas (W98), we would expect a modulation-index around 35%. This is significantly larger than the observed modulation-indices of 2.8% for image A and 1.6% for image B. Hence, the total angular size of the images must be larger than the Fresnel scale. This does, however, not exclude that part of the source might still be compact.

The variability time scale for a point source is given by (Narayan 1992)

$$t_{\rm p} = \frac{3.3}{v_{30}} \times \sqrt{\frac{\nu_0}{\nu}}\ {\rm h}, \quad (2)$$

where v_{30} is the transverse velocity of the scintillation pattern with respect to the line-of-sight to the source in units of 30 km s^{-1}. Inserting the values for the observing frequency (ν), the transition frequency (ν_0) and v_{30}=1.0, a time scale around 2 h is found, which is much smaller than the apparent variability time scales of days to weeks seen in a significant fraction of the light curves (Figs. 1–2).

If 5 to 10% of the flux density of the source is contained in a compact region ($\lesssim\theta_{\rm F}$), the rms fluctuations decreases to the observed modulation-index of 2–3% for B1600+434–A and B. The variability time scale would still remain $\sim$2 h. We have observed B1600+434 with the WSRT at 5 GHz during several 12 h periods and find no evidence for short-term variability $\gtrsim$2% over a $\lesssim$12 h time scale (Koopmans et al. in prep.). This excludes the posibility that the longer time-scale variations are purely the result of undersampled light curves. Hence, a simple compact source structure, embedded in a more extended non-scintillating region of emission, can not explain the observed variability. A more extended source ($\gg\theta_{\rm F}$) is therefore required, if we want to explain the observed modulation-index in terms of scintillation.

In case the source is extended, with a size $\theta_{\rm s}$>$\theta_{\rm F}$, both the modulation-index and variability time-scale change. The modulation-index decreases as follows (Narayan 1992)

$$m = m_{\rm p} \times \left(\frac{\theta_{\rm F}}{\theta_{\rm s}}\right)^{7/6}, \quad (3)$$

whereas the time scale of variability increases as

$$t = t_{\rm p} \times \left(\frac{\theta_{\rm s}}{\theta_{\rm F}}\right). \quad (4)$$

Combining these two equations, using the transition and observing frequencies for B1600+434, gives the relation

$$m = \left(\frac{0.90^{\rm h}}{v_{30}\cdot t}\right)^{7/6}, \quad (5)$$

for $t \gtrsim t_{\rm p} \approx 2.25^{\rm h}/v_{30}$.

If the lensed source has an angular radius of about 40 μas, the modulation-index reduces to 2–3%, as observed. The variability time scale should then be around 1 day, still significantly smaller than the observed modulation timescale in a major part of the light curves. Although part of the very short-term ($\lesssim$ few days) variability could be due to scintillation, many of the long-term variations seen in Figs. 1–2 certainly can not be explained this way.

The relatively nearby extragalactic radio source J1819+387 has a modulation-index $m\approx$0.5 and a variability time scale $t\approx$0.5–1 hour (Dennett–Thorpe & de Bruyn 2000). Using the relation between m and t (e.g. Eq. (5)), this translates to a variability time scale less than a day for a modulation-index of a few percent, in agreement with expectations from the Galactic ionized ISM model from TC93. Similarly, variations with a time scale of more than a week (Figs. 1–2) require a source size of 0.3 mas, reducing the modulation-index to 0.2%, which is well below the noise level in the VLA 8.5–GHz light curves.

In Fig. 5, we have summarized the weak and strong scattering regimes, as functions of the modulation-index, the variability time scale and the source size. The variability seen in image A (but also image B) is especially hard to explain by weak scattering without either invoking unlikely high values for the equivalent distance of the phase screen ($\gtrsim$10 kpc) or a persistently low transverse velocity ($\lesssim$few km s^{-1}). From this, we conclude that weak scattering has great difficulties in accounting for the observed modulation-indices and longer variability time scales ($\gg$1 day) seen in the VLA 8.5–GHz light curves of the lensed images. However, it remains difficult to

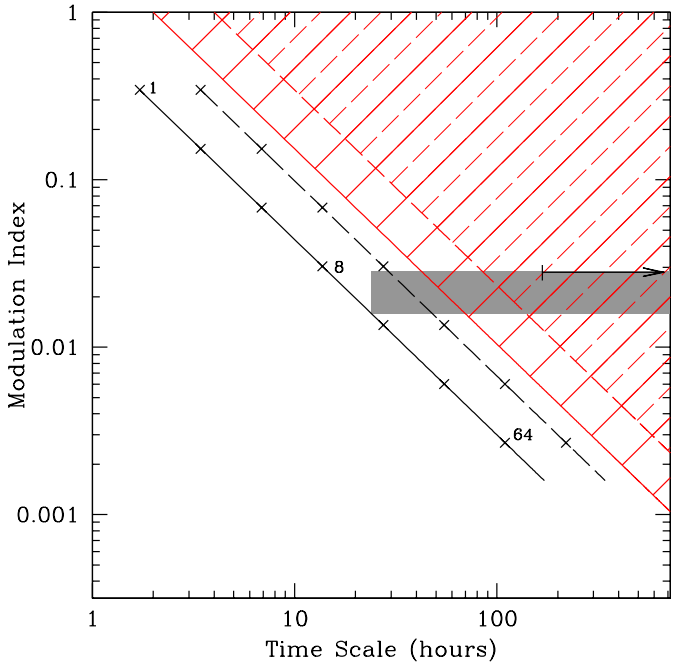

Fig. 5. The modulation-index as a function of the variability time scale for the weak scattering regime (Eq. (5)), using a transverse velocity v=40 km s^{-1} (solid line) or 20 km s^{-1} (dashed line). The short dashes perpendicular to the lines indicate different source sizes (i.e. 1, 2, 4,..., 64 in units of the first Fresnel zone, i.e. 3.9 μas). The skewed dashed regions in the upper-right corner indicate the strong scattering regime ($\xi > 1$) for the two transverse velocities, using an equivalent phase-screen distance of 0.5 kpc. The gray region indicates a variability time scale of 1–30 days and a modulation-index range of 1.6–2.8%, as observed for the lensed images. The arrow indicates the observed 2.8% modulation-index and time scale $\geq$1 week as seen in the difference light curve (Fig. 2). Only for an equivalent phase screen distance $\geq$10 kpc (with v=30 km s^{-1}) or a transverse velocity $\leq$few km s^{-1} (with D=0.5 kpc) does most of the gray region enter the weak scattering regime.

determine a reliable variability time scale from the image light curves, partly because of the relatively poor sampling (i.e. every 3.3 days). In any case, sigificant variability on short time scales ($\lesssim$12 h) is excluded (see above). For further discussion we refer to Sect. 3.2, where we present the structure functions of the observed variations.

3.2. Strong scattering

In the strong scattering regime, we can not use the numerical results derived from the TC93 model, from which one expects B1600+434 to be in the weak-scattering regime at 8.5 GHz. We therefore make direct use of the relation between the scattering measure (SM), the distance to the equivalent phase screen ($D_{\rm kpc}$), the observing frequency ($\nu_{\rm GHz}$) and the scattering strength (ξ) (e.g. W98)

$$\xi = 2.6 \cdot 10^3 \times {\rm SM}^{6/10} D_{\rm kpc}^{1/2}\, \nu_{\rm GHz}^{-17/10}. \quad (6)$$

The scattering strength and the Fresnel scale determine both the modulation-index and variability time scale of a source, given the source size. The Fresnel scale, given by

$$\theta_{\rm F} = 8/\sqrt{D_{\rm kpc}\nu_{\rm GHz}}\ \ \mu{\rm as}, \quad (7)$$

specifies the angular distance from the source over which there is about one radian phase difference between rays, due to the difference in path length. The scattering measure (e.g. TC93) for an extra-galactic source is defined as

$${\rm SM} = \int_0^\infty C_{\rm n}^2 {\rm d}l, \quad (8)$$

where $C_{\rm n}^2$ is the structure constant normalizing the Kolmogorov power-law spectrum of the ionized ISM inhomogeneities (e.g. Cordes, Weisberg & Boriakoff 1985). From now on, we assume that SM has units of kpc m$^{-20/3}$ and $C_{\rm n}^2$ units of m$^{-20/3}$. The distance to the equivalent phase screen (e.g. W98) is defined as

$$D \equiv \frac{1}{\rm SM}\int_0^\infty C_{\rm n}^2 \cdot s\ {\rm d}s. \quad (9)$$

Despite the fact that the difference in modulation-index of the lens images seems to require very different properties of the Galactic ionized ISM on a scale of 1.4 arcsec, we will investigate the two distinct strong scattering regimes, i.e. refractive and diffractive (e.g. Rickett 1990; Narayan 1992), in more detail in the next two sections.

3.2.1. Refractive scintillation

Using Eq. (6) and the scaling laws from Narayan (1992), one finds for a point source in the strong scattering regime that the modulation-index is

$$\begin{aligned} m_{\rm p} &= \xi^{-1/3} \\ &\approx 7.3 \cdot 10^{-2} \cdot {\rm SM}^{-1/5}\, D_{\rm kpc}^{-1/6}\, \nu_{\rm GHz}^{17/30}, \end{aligned} \quad (10)$$

whereas the variability time scale is

$$t_{\rm p} = \frac{\theta_{\rm F} D}{v}\xi \approx \frac{3.3}{v_{30}}\, D_{\rm kpc}\, {\rm SM}^{6/10}\, \nu_{\rm GHz}^{-11/5}\ {\rm yrs}. \quad (11)$$

We furthermore use $D_{\rm kpc}$=0.5 (TC93), v_{30}=1.0 and $\nu_{\rm GHz}$=8.5 throughout this section. From Eqs. (10–11) it is immediately obvious that for a point source in the refractive regime, an extremely high value for SM is needed ($\gtrsim 10^5$ kpc m$^{-20/3}$) to obtain the modulation-index of images A and B. The time scale of variability would be around 15 years. Clearly the point-source approximation is not valid.

For extended sources, the modulation-index and time scale of variability scale as $(\theta_{\rm r}/\theta_{\rm s})^{7/6}$ and $(\theta_{\rm s}/\theta_{\rm r})$, respectively, where $\theta_{\rm s}$ is the source size and $\theta_{\rm r}$ the size of the scattering disk (Narayan 1992). At 8.5 GHz, we find

$$\theta_{\rm r} = \theta_{\rm F} \cdot \xi \approx 180 \times {\rm SM}^{6/10}\ \ \mu{\rm as}, \quad (12)$$

which is independent of the distance to the equivalent phase screen. If we subsequently use the scaling laws, combined with

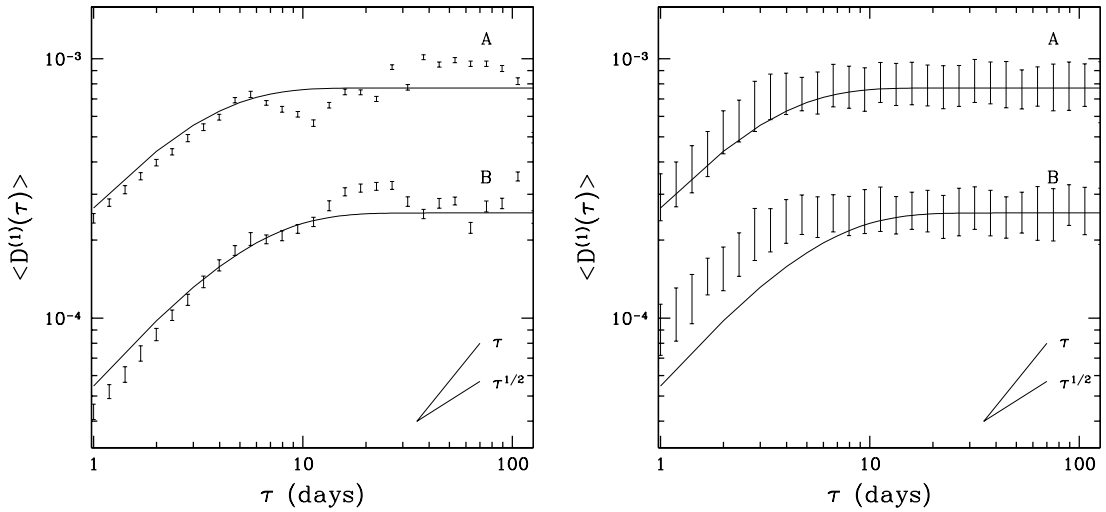

Fig. 6. *Left:* The structure functions of the normalized light curve of images A and B. The solid curves shows the expected structure functions, derived as in BNR86, assuming a scale length of 0.9 kpc for the Gaussian distribution of the ionized scattering medium and v=30 km s^{-1}. Fits are only obtained for very different source sizes of 62 and 108 μas for images A and B, respectively. The 1–σ error bars on the structure functions are derived from Monte-Carlo simulations. *Right:* The simulated structure functions of the normalized light curve of images A and B, replacing the observed normalized flux densities at each epoch with a random Gaussian distributed value with a 1–σ scatter equal to the observed modulation-index in the light curves, i.e. 2.8% and 1.6% for images A and B, respectively

Eqs. (10–11), we find a relation between the time scale of variability and the modulation-index:

$$m = \xi^{5/6} \left(\frac{\theta_{\rm F} D}{v \cdot t} \right)^{7/6}, \quad (13)$$

which is valid only if $\theta_{\rm s} > \theta_{\rm r}$. Inserting the usual numerical values for v, D and ν, we find

$$m \approx 2.0 \cdot {\rm SM}^{1/2}\, t_{\rm d}^{-7/6}, \quad (14)$$

with $t_{\rm d}$ in units of days. We find that a scattering measure SM$\gtrsim 2 \cdot 10^{-2}$ is needed to explain modulations with a time scale of $\gtrsim$1 week in image A. From TC93 we find that SM=$2 \cdot 10^{-4}$ in the direction of B1600+434, corresponding to a time scale of one day. For deep modulations of about 1 month a scattering measure SM$\approx$0.5 is needed for image A. Both values are larger than can be expected on the basis of the ionized ISM model from TC93.

Differences in the scattering measure: A strong argument against refractive scattering is the large difference between the modulation-indices of images A and B. If this is due to a difference in the scattering measure, it requires ${\rm SM_A/SM_B} \approx (0.028/0.016)^2 \approx 3.1$ (Eqs. (13–14)), which is substantial over an angular scale of only 1.4 arcsec. The same factor is found for the weak-scattering regime.

The structure function: We have also calculated the structure function (SF; Simonetti et al. 1985):

$$\mathrm{D}^{(1)}(\tau) = \frac{1}{2} < (\delta \mathrm{F}(t) - \delta \mathrm{F}(t+\tau))^2 >, \quad (15)$$

following Blandford, Narayan & Romani (1986 [BNR86]), who investigated intensity fluctuations (i.e. "flickering") of extended radio sources, caused by refractive scattering. $\mathrm{F}(t)$ is the normalized light curve as shown in Fig. 1. BNR86 take a slightly steeper spectrum of the phase fluctuations with a power-spectrum slope β=4, instead of a Kolmogorov slope of β=11/3.

Fitting the theoretical SF from BNR86 to the observed SFs[1] (Fig. 6) gives a scale length of $L \sim$0.9 kpc, which corresponds to an equivalent phase screen distance of $0.9/\sqrt{\pi}$ $\approx$0.5 kpc (Eq. (9)). The 'best-fit' image sizes are 62 and 108 μas, respectively, for images A and B. The saturation time scales (e.g. BNR86) found from these fits are $\tau_{\rm s}^{\rm A}$=2.5 days and $\tau_{\rm s}^{\rm B}$=4.4 days, even though there are clear variations with longer time scales in the light curves. The presence of variabilty with longer time scales ($\gtrsim$week) has been confirmed by new multi-frequency VLA observations in 1999/2000 (Koopmans et al. in prep.).

To test the reliability of these saturation time scales, we replaced the normalized flux densities at each epoch in Fig. 1 by Gaussian–distributed values with a 1–σ scatter equal to the observed modulation-index of the light curve. In Fig. 6 the result is shown, from which it is immediately clear that the light curves are undersampled such that the SFs and the saturation time scales for time lags $\tau \lesssim$4 days become highly unreliable.

Scatter-broadening: The difference between the modulation-indices of images A and B can be explained by a difference in the scattering measure of the Galactic ionized ISM towards

[1] The structure function $\mathrm{D}^{(1)}(\tau)$, calculated from the normalized light–curves, corresponds to the structure function $\mathrm{D}^{(2)}(\tau)$, calculated from the observed light curves (KBXF00), because SFs of order M remove polynomials of order M–1 from the time series (e.g. Simonetti et al. 1985).

both images, as well as by a difference in their respective image sizes (see above). However, image B has a smaller magnification due to the lensing potential and should therefore be smaller than image A. Consequently, image B should show stronger variability than image A, whereas it does not. The only viable alternative to obtain a larger size for image B is through scatter-broadening by the ionized ISM in the lens galaxy.

The expected scattering disk at 8.5 GHz due to the Galactic ionized ISM is $\sim$1 μas and cannot account for the apparent difference in the image size, derived from the SFs. This requires a scattering disk of $\gtrsim$90 μas for image B at 8.5 GHz, if image A is not scatter-broadened, implying that $\mathrm{SM_B}\approx$1 in the lens galaxy. If we take into account that scattering occurs at a frequency of $8.5\times(1+z_{\rm l})\approx$12.0 GHz, this implies a scattering disk of 3 mas at 1.7 GHz, which is nearly equal to the very conservative upper limit of $\lesssim$4 mas on the image sizes found from 1.7–GHz VLBA observations (Neal Jackson, private communication).

Recent polarization observations by Patnaik et al. (1999) gave rotation measures RM=40 rad m^{-2} and has RM=44 rad m^{-2} for images A and B, respectively. The difference of 4$\pm$4 rad m^{-2} is rather low and certainly does not support a high scattering measure in the disk/bulge of the lens galaxy.

Hence, although scatter-broadening cannot be excluded, to fully explain the observed difference between the modulation-indices of images A and B in terms of galactic scintillation, one would require an extremely high scattering measure in the lens galaxy.

3.2.2. Diffractive scintillation

For diffractive scintillation at 8.5 GHz to be at work, one requires both a very high scattering measure and a very small source, neither of which seems plausible. However, to be complete we briefly discuss this possibility.

The modulation-index is unity for a point source,

$$m_{\rm p} = 1, \tag{16}$$

much larger than seen in both lensed images. However, for a source larger than the scale on which there are phase changes of about 1 radian ($\theta_{\rm d}$), the modulation-index becomes $m = (\theta_{\rm d}/\theta_{\rm s})$, where $\theta_{\rm s}$ is the source size. We find (e.g. W98)

$$\begin{aligned}\theta_{\rm d} &= \theta_{\rm F}\,\xi^{-1} \\ &\approx 3.1\cdot10^{-3}\cdot\mathrm{SM}^{-6/10}\nu_{\rm GHz}^{6/5}D_{\rm kpc}^{-1}\ \mu\mathrm{as},\end{aligned} \tag{17}$$

and for the point–source variability time–scale

$$t_{\rm d} = t_{\rm F}\cdot\xi^{-1} \approx \frac{0.25}{v_{10}}\cdot\mathrm{SM}^{-6/10}\nu_{\rm GHz}^{6/5}\ \mathrm{min}, \tag{18}$$

where $t_{\rm F}$=$\theta_{\rm F}Dv^{-1}$=$4.0\cdot10^4\cdot v_{30}^{-1}\sqrt{D_{\rm kpc}/\nu_{\rm GHz}}$ sec. The time scale increases by $(\theta_{\rm s}/\theta_{\rm d})$, if the source size is larger than $\theta_{\rm d}$. Combining the equations above, we find the relation

$$\xi = \frac{t_{\rm F}}{m\cdot t}, \tag{19}$$

where m is the observed modulation-index. This relation is independent of source size, as long as the source is larger than the diffractive scale $\theta_{\rm d}$. Using this equation, we immediately find that $\theta_{\rm d} > \theta_{\rm F}$ for the deep modulations of $\gtrsim$1 week, which is only true in the weak scattering regime. Thus, diffractive scattering offers no solution either, which comes as no surprise.

4. Radio microlensing: theory

Microlensing is unlikely for bright ($\gtrsim$1 Jy) flat-spectrum radio sources at low frequencies ($\sim$few GHz), which have typical angular sizes of $\gtrsim$1 mas, determined by the inverse Compton limit on their surface brightness (e.g. Kellerman & Pauliny–Toth 1969). This angular size is much larger than the typical separation of a few μas between caustics in the magnification pattern, thereby reducing any significant microlensing variability (see Sect. 5).

High-frequency ($\sim$10 GHz) sources with flux densities less than a few tens of mJy, however, can be as small as several tens of μas. If part of the source is moving with relativistic velocities ($\beta_{\rm app}c$), Doppler boosting allows an even smaller angular size. In those cases, microlensing can start to contribute significantly to the short-term variability seen in these sources (e.g. Gopal-Krishna & Subramanian 1991).

This is in stark contrast to optical microlensing, where the variability time scales are dominated by the transverse velocity ($v_{\rm trans}$) of the galaxy with respect to the line-of-sight to the static source, as in the case of Q2237+0305 (e.g. Wyithe, Webster & Turner 1999). Microlensing time scales between strong caustic crossings in the optical waveband are therefore several orders of magnitude (i.e. $\beta_{\rm app}c/v_{\rm trans}\sim10^3$) larger than in the radio waveband. This makes superluminal radio sources the perfect probes to study microlensing by compact objects in strong gravitational lens galaxies, using relatively short ($\lesssim$1 year) monitoring campaigns.

4.1. Relativistic jet-components

If the lensed source consists of a static core and a synchrotron self-absorbed jet-component, which moves away from the core with a velocity $\beta_{\rm bulk}$=v/c, the Doppler factor of this jet-component is given by

$$\mathcal{D} = [\gamma\ (1-\boldsymbol{\beta}_{\rm bulk}\cdot\boldsymbol{n})]^{-1}, \tag{20}$$

where γ=$(1-\beta_{\rm bulk}^2)^{-1/2}$ and $\boldsymbol{n}$ is the direction of the observer (e.g. Blandford & Königl 1979).

The observed flux density of a circular-symmetric radio source with an observed angular radius $\Delta\theta$ is

$$S(\nu) = \frac{2kT_{\rm b}\nu^2}{c^2}\cdot\pi\Delta\theta^2, \tag{21}$$

where ν is the observing frequency and $T_{\rm b}$ the observed brightness temperature of the source. We assume the source has a constant surface brightness. However, due to the Doppler boosting, the apparent brightness temperature of a relativistic jet–component moving towards the observer can be significantly

brighter than the inverse Compton limit of about $T_{\rm b,ic}{\approx}5{\cdot}10^{11}$ K (e.g. Kellerman & Pauliny-Toth 1969). The true comoving surface brightness temperature of a flat-spectrum radio source is related to the observed surface brightness temperature ($T_{\rm b}$) through

$$T_{\rm b} = 10^{12} \times T_{12}^{\rm b,ic} \left(\frac{\mathcal{D}}{1+z} \right) \ {\rm K}, \tag{22}$$

where z is the redshift of the source (e.g. Blandford & Königl 1979). If we substitute Eq. (22) into Eq. (21), we find that the flux density of the relativistically moving jet-component is

$$S_{\rm knot} = 0.23 \left[\frac{\mathcal{D}\, T_{12}^{\rm b,ic}}{1+z} \right] \nu_{10}^2 \left(\frac{\Delta\theta_{\rm knot}}{\mu{\rm as}} \right)^2 \ {\rm mJy}, \tag{23}$$

with ν=10$\cdot\nu_{10}$ GHz. Inverting this equation, we find an approximate angular radius of the jet-component

$$\Delta\theta_{\rm knot} = 2.1 \cdot \left[\left(\frac{S_{\rm knot}}{\rm mJy} \right) \frac{(1+z)}{\mathcal{D}\, T_{12}^{\rm b,ic} \nu_{10}^2} \right]^{1/2} \ \mu{\rm as}. \tag{24}$$

Given the observed frequency, the redshift of the jet-component and the Doppler boosting $\mathcal{D}$, we can subsequently set a limit on the angular radius of the jet-component.

In the case of B1600+434, the redshift of the lensed quasar is z=1.59 (Fassnacht & Cohen 1998). The observing frequency is ν_{10}=0.85 and $S_{\rm knot}{\approx}S_{8.5}^{\rm tot}\cdot f$, where f is the fraction of the total average source flux density in the relativistic jet-component, $S_{8.5}^{\rm tot}{\approx}25/\langle\mu\rangle$ mJy (KBXF00) and $\langle\mu\rangle$ is the average magnification at the image position. From the singular isothermal ellipsoidal (SIE) mass model (Kormann, Schneider & Bartelmann 1994), we find $\langle\mu_{\rm A}\rangle{\approx}1.7$ (κ=0.2) and $\langle\mu_{\rm B}\rangle{\approx}1.3$ (κ=0.9). We use $\langle\mu\rangle{\approx}1.5$ as a typical value.

After inserting all the known observables into Eq. (24) and adopting $T_{12}^{\rm b,ic}$=0.5, we find an approximate relation between the fraction of the total observed flux–density of B1600+434 contained in the jet–component and its angular size in the source plane

$$\Delta\theta_{\rm knot} \approx 20 \cdot \sqrt{\frac{f}{\mathcal{D}}} \ \mu{\rm as}. \tag{25}$$

This equation can be used to put constraints on the light-curve fluctuations seen in B1600+434, and decide whether they are the result of microlensing of a single relativistic jet-component.

4.2. Microlensing time scales

The typical time scale which one would expect between relatively strong microlensing events is the angular separation between strong caustic crossings divided by the angular velocity of the jet-component in the source plane.

In case the source is not lensed, the apparent velocity (in units of c) of the jet-component is

$$\boldsymbol{\beta}_{\rm app} = \frac{\boldsymbol{n} \times (\boldsymbol{\beta}_{\rm bulk} \times \boldsymbol{n})}{1 - \boldsymbol{\beta}_{\rm bulk} \cdot \boldsymbol{n}} = \frac{\boldsymbol{\beta}_{\rm bulk} \sin(\psi)}{1 - |\boldsymbol{\beta}_{\rm bulk}| \cos(\psi)}, \tag{26}$$

where ψ is the angle between the jet and the line–of–sight and $\beta_{\rm bulk}$ the bulk velocity of the jet–component (e.g. Blandford & Königl 1979). The apparent angular velocity (in vector notation) of the jet–component becomes

$$\begin{aligned} \frac{{\rm d}\boldsymbol{\theta}_{\rm s}}{{\rm d}t} &= \frac{\boldsymbol{\beta}_{\rm app} c}{(1+z_{\rm s}) D_{\rm s}} \\ &= \frac{1.2 \cdot \boldsymbol{\beta}_{\rm app}}{(1+z_{\rm s})} \left(\frac{D_{\rm s}}{\rm Gpc} \right)^{-1} \ \frac{\mu{\rm as}}{\rm week}, \end{aligned} \tag{27}$$

where $z_{\rm s}$ and $D_{\rm s}$ are the redshift and the angular diameter distance to the stationary core, respectively. If the jet-component moves with superluminal velocities ($\beta_{\rm app} \geq 1$), one expects angular velocities in the order of several tenths of μas per week. Because the source is lensed by the foreground galaxy, its observed angular velocity (in the lens plane) becomes

$$\frac{{\rm d}\boldsymbol{\theta}_{\rm d}}{{\rm d}t} = \left[\mathcal{A}^{-1} \cdot \frac{{\rm d}\boldsymbol{\theta}_{\rm s}}{{\rm d}t} \right] \left(\frac{D_{\rm d}}{D_{\rm s}} \right), \tag{28}$$

where

$$\mathcal{A} = \begin{bmatrix} 1-\kappa-\gamma_1 & -\gamma_2 \\ -\gamma_2 & 1-\kappa+\gamma_1 \end{bmatrix} \tag{29}$$

is the local transformation matrix of the source plane to the lens plane, with κ and $\gamma_{1,2}$ being the local convergence and shear (e.g. Gopal-Krishna & Subramanian 1991; Schneider et al. 1992).

We calculate the source and caustic structure in the source plane, however. Thus, the angular velocity and source structure undergo the inverse transformation of the angular velocity in the source plane (Eq. (28)). The angular velocity that we need to use, is therefore given by Eq. (27). Using the observed redshift z=1.59 (Fassnacht & Cohen 1998) of B1600+434 the angular velocity in the source plane reduces to

$$\frac{{\rm d}\boldsymbol{\theta}_{\rm s}}{{\rm d}t} = 0.34 \cdot \boldsymbol{\beta}_{\rm app} \ \frac{\mu{\rm as}}{\rm week}, \tag{30}$$

where we assume a flat Friedmann–Robertson–Walker universe with $\Omega_{\rm m}$=1 and H_0=65 km s^{-1} Mpc^{-1}.

4.3. Microlensing modulation-indices

The normalized modulation-index (m_μ) of a superluminal jet component, due to microlensing, is

$$m_\mu \equiv \sqrt{\frac{\langle\mu^2\rangle}{\langle\mu\rangle^2} - 1}, \tag{31}$$

where μ=$\mu(t)$ is the microlensing light curve of the jet component. We determine m_μ as function of the angular size of the source by averaging over randomly-oriented simulated microlensing light curves and find that m_μ can be well approximated by the analytical function

$$m_\mu(\Delta\theta_{\rm knot}) = \frac{C_\mu}{1 + \left(\frac{\Delta\theta_{\rm knot}}{\Delta\theta_{\rm b}} \right)} \tag{32}$$

for $\Delta\theta_{\rm knot}\lesssim 20\mu$as, where $\Delta\theta_{\rm b}$ is the turnover size of the source after which the modulation-index m_μ decreases linearly with source size and C_μ is the asymptotic modulation-index for a source with $\Delta\theta_{\rm knot}\rightarrow 0$. We fit this function to the numerical results to obtain both C_μ and $\Delta\theta_{\rm b}$.

We subsequently combine Eqs. (25) and (32) with the fact that the observed modulation-index in the lensed images is $m_\mu^{\rm obs}=f\cdot m_\mu$ and find

$$m_\mu^{\rm obs}(f,\mathcal{D})\approx\frac{C_\mu\cdot f}{1+20\ \Delta\theta_{\rm b}^{-1}\ \sqrt{f/\mathcal{D}}}, \quad (33)$$

where $\Delta\theta_{\rm b}$ is in units of μas.

Many jets consist of more than a single jet-component. If we assume that (i) the jet consists of N similar jet-components, each containing a fraction f_1=f/N of the total flux–density and (ii) the magnification curves of the jet-components to be uncorrelated, we expect the modulation-index of the combined jet-components to decrease roughly as $\sim 1/\sqrt{N}$. Hence, we find that $m_\mu^{\rm obs}(N)\approx\cdot f\cdot m_\mu(f_1)/\sqrt{N}$, or

$$m_\mu^{\rm obs}(f,\mathcal{D})\approx\frac{C_\mu\cdot f/\sqrt{N}}{1+20\ \Delta\theta_{\rm b}^{-1}\ \sqrt{f/(\mathcal{D}N)}}, \quad (34)$$

where f=$N\ f_1\leq 1$. Hence, multiple jet-components will in general decrease the modulation-index. However, if the individual jet-components are very compact – i.e. are much smaller than the typical separation between strong caustics –, the microlensing variability will be dominated by single caustic crossings, creating strong isolated peaks in the light curve. We then expect Eq. (34) to break down, such that the factor $1/\sqrt{N}$ in the numerator can be removed.

In the case of scintillation, N compact jet-components ($\Delta\theta_{\rm knot}\lesssim\theta_{\rm F}$) always vary independently, such that the observed modulation-index roughly decreases as $1/\sqrt{N}$. However, in the case of microlensing, the modulation-index, caused by the same compact jet-components moving over a magnification pattern, can be independent from N or even increase as $\sqrt{N}$.

4.4. Source constraints

At this point, we give a qualitative recipe to obtain constraints on the jet-component parameters from the observed light curves.

1. First, the observed modulation-indices of both lensed images can be used to solve for the fraction of flux density in the jet-component (f), as well as its Doppler factor ($\mathcal{D}$), by comparing them to those found from numerical simulations for different mass functions (MFs), which fix both C_μ and $\Delta\theta_{\rm b}$). One obtains a set of two equations (i.e. Eq. (33)) with two constraints ($m_\mu^{\rm A}$ and $m_\mu^{\rm B}$) and two unknown variables ($\mathcal{D}$ and f), which in some cases can be uniquely solved for. The combinations of MFs, which do not give a consistent solution, can be excluded, thereby putting constraints on the allowed MFs in the line-of-sight towards the lensed images.
2. Second, combining the typical observed variability time scale between strong microlensing events and the angular separation of these from the numerical simulations, one can obtain a value for $\beta_{\rm app}$ (Eq. (27)). Combining Eqs. (20) and (26), one then also readily solves for both ψ and $\beta_{\rm bulk}$.

Thus, given (i) a mass model of the lens galaxy found from (macroscopic) lens modeling, (ii) some plausible range of MFs near the lensed images and (iii) the observed modulation-indices and variability time scales in the light curves of the lensed images, one can in principle solve for several parameters of the simple jet/jet–component structure: $\mathcal{D}$, f, ψ, $\beta_{\rm app}$, $\beta_{\rm bulk}$ and $\Delta\theta$. However, one should keep in mind that some of the parameters might be degenerate and that we also do not know intrinsic brightness temperature of the components.

5. Radio microlensing: results

In this section, we examine the observed variability in the light curves of B1600+434 A and B in terms of microlensing and, following the procedure delineated in Sect. 4.4, derive constraints on the properties of the jet-component, as well as on the MFs near both lensed images. In Sect. 7, we will use these results to determine the microlensing modulation-index as function of frequency and compare this to the results from independent WSRT 1.4 and 5–GHz monitoring data of B1600+434 (Sect. 2). An overview of the combined microlensing/scintillation situation in B1600+434 is given in Fig. 8, which might act as guide to the overall situation.

From now on, we will (i) use a source structure consisting of a static core plus a *single* relativistically moving spherically-symmetric jet-component, (ii) assume that the core and jet parameters do not change appreciably over the time-span of the observations, (iii) assume that *all* short-term variability in the image light curves (Fig. 1) is dominated by microlensing and that scatter-broadening is negligible. The static core does not contribute to the short-term variability, because its velocity with respect to the magnification pattern of the lens is much smaller than that of the jet-component (i.e. $v_{\rm core}\ll v_{\rm jet}$). At this moment, we feel that a more detailed model is not warranted. One should, however, keep in mind that the conclusions drawn below depend on these assumptions !

5.1. Numerical simulations

From KBJ98, we find for B1600+434 that the local convergence and shear are close to κ=γ=0.2 for image A, using a singular isothermal ellipsoidal (SIE) mass distribution for the lens galaxy. Similarly for image B, we find κ=γ=0.9. Using these input parameters, we simulate the magnification pattern of a $50\,\eta_{\rm e}\times 50\,\eta_{\rm e}$ field for different MFs, where $\eta_{\rm e}$ is the Einstein radius of a 1–M$_\odot$ star projected on the source plane. We use the microlensing code developed by Wambsganss (1999). Using the lens redshift $z_{\rm l}=0.41$, the source redshift $z_{\rm s}$=1.59 and H$_0$=65 km s^{-1} Mpc^{-1} in a flat ($\Omega_{\rm m}$=1) FRW universe, we find that $\eta_{\rm e}$=2.1 μas. The magnification pattern is calculated on a grid of 1000$\times$1000 pixels. Each pixel has a size of 0.107 μas by 0.107 μas.

Table 2. Summary of the modulation-index caused by microlensing as a function of source size for the power-law MFs (BP1–4) near image B and the single-mass MFs (AS1–9 and BS1–7) near images A and B

MF	Mass ($M_\odot$)	Slope	$\langle M \rangle$ ($M_\odot$)	C_μ	$\Delta\theta_{\rm b}$ (μas)
A					
S1	0.1	–	–	0.69	0.94
S2	0.2	–	–	0.70	1.28
S3	0.4	–	–	0.71	1.87
S4	0.6	–	–	0.69	2.44
S5	0.8	–	–	0.70	2.48
S6	1.0	–	–	0.71	2.71
S7	1.5	–	–	0.71	3.07
S8	2.5	–	–	0.69	4.27
S9	5.0	–	–	0.76	4.50
B					
S1	0.1	–	–	1.00	0.90
S2	0.2	–	–	1.01	1.17
S3	0.4	–	–	1.03	1.41
S4	0.6	–	–	1.05	1.98
S5	0.8	–	–	1.06	2.35
S6	1.0	–	–	1.07	2.65
S7	1.5	–	–	1.12	2.95
P1	0.01–1	-2.35	0.031	1.01	1.09
P2	0.01–1	-1.85	0.058	1.05	1.37
P3	0.01–1	-2.85	0.021	0.98	0.71
P4	0.1–10	-2.35	0.309	1.09	2.00

We simulate 100 randomly-oriented light curves on this grid, for a range of jet-component sizes ($\Delta\theta_{\rm knot}$=0.125, 0.25,..., 16.0 μas) and MFs for the compact objects (see Sect. 5.2). Each simulated light curve is 54 μas long. For each step (5 pixels) on the light curve, we calculate the magnification of a circular-symmetric jet-component with a constant surface-brightness and a radius $\Delta\theta$, by convolving the magnification pattern with its surface-brightness distribution (e.g. Wambsganss 1999).

We also assume that the surface density near image B is dominated by stellar objects in disk and bulge of the lens galaxy, even though the halo does contribute to the line-of-sight surface density. If we assume that the halo surface density near image B is equal to that near image A (κ=0.2), the density of the caustics in the resulting magnification pattern remains completely dominated by the significantly higher number density of compact objects in the disk and bulge (κ=0.7). We have tested this by modifying the microlensing code to allow multiple mass functions. The rms variabilities calculated from these modified magnification patterns are the same within a few percent from those without the halo contribution (for the range of mass functions and surface densities that we used in this paper), which justifies this simplification.

5.2. The mass function of compact objects in the lens galaxy of B1600+434

We use a range of different MFs, subdivided in two classes: (i) power-law MFs and (ii) single-mass MFs.

5.2.1. The power-law MF

In the solar neighborhood it appears that the stellar MF can be represented by a single or segmented power-law of the form $\mathrm{d}N(m)/\mathrm{d}M \propto M^\alpha$ (e.g. Salpeter 1955; Miller & Scalo 1979). Recent observations towards the Galactic bulge (e.g. Holtzman et al. 1998) suggest a break in the MF around 0.5–0.7 $M_\odot$, with a shallower slope at lower masses. A lower-mass cutoff is not well constrained, although the break in the MF suggests it might lie around a few tenths of a solar mass. Evolution of the MF from z=0.4 to z=0.0 affects the upper mass cutoff only and has no significant influence on microlensing, which is dominated by the mass concentrated around the lower mass cutoff.

1. First, we simulate the magnification pattern, using a power-law MF with $\alpha = -2.35$ (Salpeter 1955) and a mass range between 0.01–1.0 $M_\odot$.
2. Second, we also investigate the slopes -2.85 and -1.85 for image B – going through the bulge/disk – assuming again a mass range of 0.01–1 $M_\odot$.
3. Third, we use an MF mass range of 0.1–10 $M_\odot$ near image B, with a slope of -2.35. This gives an average stellar mass of about 0.3 $M_\odot$, more in line with observations of the bulge of our Galaxy (e.g. Holtzman et al. 1998).

We use the power-law MFs for image B only, even though it is clearly a rough approximation of the true MF. A similar power-law MF for image A, passing through the halo, seems unlikely, especially if the halo consists of stellar remnants (e.g. Timmes, Woosley & Weaver 1996).

The results from these simulations – m_μ as a function of $\Delta\theta_{\rm knot}$ – are fitted by Eq. (32). The values for C_μ and $\Delta\theta_{\rm b}$ are listed in Table 2 (models BP1–4).

5.2.2. The single-mass MF

In steep ($\alpha<-1$) MFs most of the mass is concentrated close to the lower-mass cutoff in the MF. It therefore seems appropriate to approximate the MF by a delta-function. We simulated single-mass MFs for both image A and B, for 0.1, 0.2, 0.4, 0.6, 0.8, 1.0, 1.5 $M_\odot$ and additionally for 2.5 and 5.0–$M_\odot$ for image A. The results are listed in Table 2.

From these simulation, we notice several things: First, C_μ is almost independent from the average mass of the compact objects, for a given surface density. Second, there appears to be a strong correlation between the average mass of the compact objects and the turnover angle ($\Delta\theta_{\rm b}$), which means that for a given surface density, shear and source size, the modulation-index is larger for a higher average mass of the compact objects. The results from our simulations are consistent with the results in Deguchi & Watson (1987) and Refsdal & Stabell (1991, 1997).

5.3. Microlensing in B1600+434?

As we can see from Table 2, the modulation-index in image A can be explained by a relatively small jet-component with a moderate boosting factor. However, one might expect image B

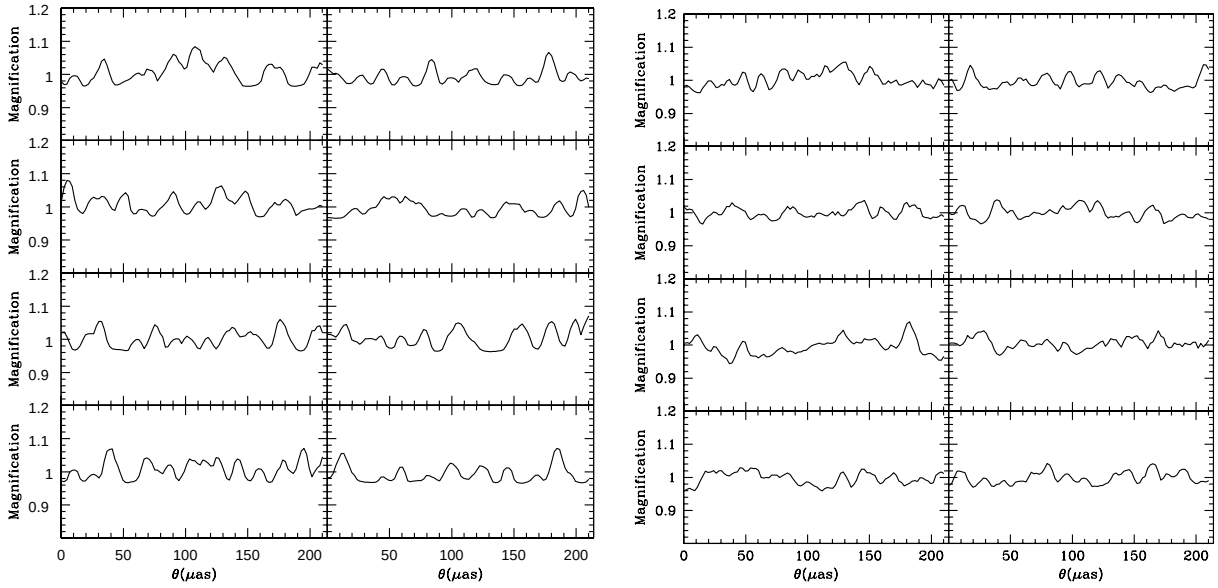

Fig. 7. *Left:* Eight arbitrary simulated light curves for a single compact 5-μas source, moving over the magnification pattern near image A. The values f and $\mathcal{D}$ from Table 3 were used. The simulated curves were subsequently scaled by f. A 1.5–$M_\odot$ single–mass MF was used. The light curves were created through a convolution of the source surface–brightness distribution with the magnification pattern. The source was moved over a 500-pixels path (i.e. 214 μas), randomly placed on the magnification pattern. *Right:* Idem, for image B, using a 0.2–$M_\odot$ single-mass MF. The ratio between the modulation-index for the simulated light curves, is approximately equal to the observed ratio of modulation-indices in the observed light curves of B1600+434 A and B (Fig. 1). The scale, in this random example, would correspond to 35 weeks, the duration of the monitoring campaign of B1600+434 ($\beta_{\rm app}\approx$18).

to show similar, if not stronger variability for a similar MF. This is not the case, however. Before we examine this in terms of a different mass function in the disk/bulge and halo of the lens galaxy, we first explore two alternative explanations:

- What if the dimensionless surface density near image B is near unity (i.e. $\kappa\approx$1)? In that case, the magnification pattern can become very dense and suppress the modulation-index (e.g. Deguchi & Watson 1987; Refsdal & Stabell 1991, 1997). For B1600+434 we used $\kappa_{\rm B}\approx\gamma_{\rm B}$ (Sect. 5.1), in which case the density of the caustics remains relatively small, in contrast with the case where $\kappa\approx$1 and $\gamma\approx$0 (e.g. Refsdal & Stabell 1997). This is supported by simulations with $\kappa = \gamma = 0.999$ near image B, which give nearly the same results as for $\kappa = \gamma = 0.9$.
- In Sect. 3.2 we showed that scatter-broadening of image B can suppress scintillation caused by the Galactic ionized ISM. Similarly, is can suppress variability due to microlensing. An overview of the situation is given in Fig. 8. Image A, however, is seen through the galaxy halo at about 4 h^{-1} kpc above the disk (KBJ98). It is therefore extremely unlikely to pass through a region with a high scattering measure (Sect. 3.2). In the remainder of the paper, however, we assume that *both* images A and B are not affected by scatter-broadening (situation 2 in Fig. 8).

We will now explore the only other plausible solution; a very different MF of compact objects near images A and B.

Table 3. All combinations of the MFs (Table 2) near image A and B that give a consistent solution of the parameters: f, $\mathcal{D}$. Given these two parameters, one reproduces the observed modulation indices for both lensed images, using Eq. (33) and Table 3.

MF	AS6	AS7	AS8	AS9
BS1	–	0.09,1.3	0.07,2.1	0.05,3.4
BS2	–	0.10,1.2	0.07,2.0	0.05,3.2
BS3	–	–	0.07,1.7	0.06,2.7
BS4	–	–	0.08,1.5	0.06,2.4
BS5	–	–	0.08,1.4	0.06,2.4
BS6	–	–	0.08,1.3	0.06,2.0
BS7	–	–	–	0.07,1.4
BP1	–	0.10,1.2	0.07,2.0	0.05,3.2
BP2	–	–	0.08,1.5	0.06,2.4
BP3	0.11,1.1	0.09,1.6	0.07,2.5	0.05,4.0
BP4	–	–	0.08,1.1	0.06,1.8

5.3.1. Limits on the MF and source structure

In Table 3, we have listed all combinations between the simulated MFs for images A and B (Table 2) that reproduce the observed short-term modulation-indices of 2.8% (A) and 1.6% (B) for a consistent set of parameters f and $\mathcal{D}$ (Sect. 4.4). Several examples of simulated light curves are shown in Fig. 7.

Constraints on the MFs in B1600+434: From Table 3 one finds that a significantly higher average mass of compact objects in the halo is needed than in the bulge/disk to explain the

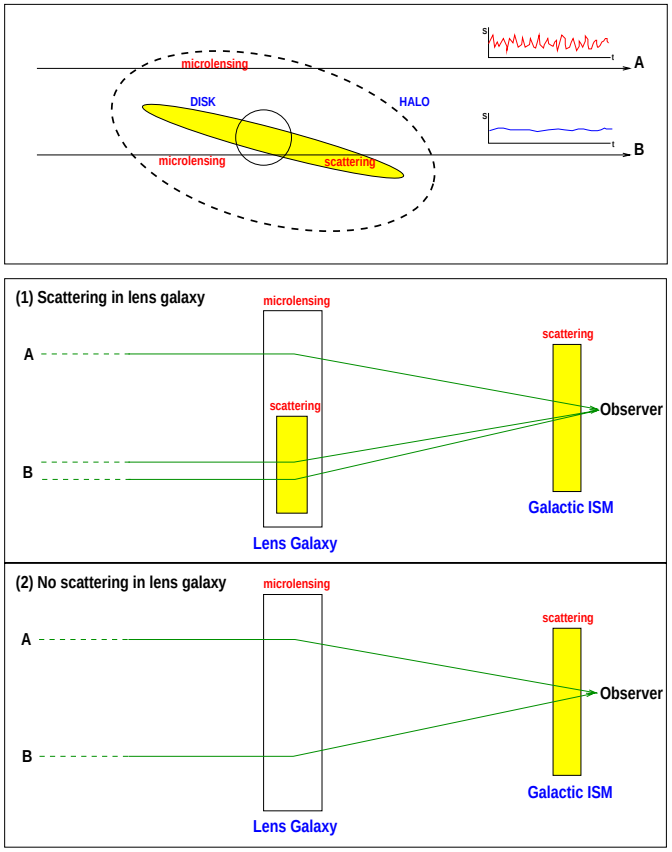

Fig. 8. The overall microlensing and scattering situation in B1600+434, when seen 'side-ways'. The inclination of the disk has been slightly exaggerated (i=75°). Situation 1: Light coming from image A passes predominantly through the halo. Light coming from image B first passes through the bulge/disk, where the image might be scatter-broadened by the lens–galaxy ionized ISM (Sect. 3.2). The image subsequently subtends a larger solid angle, suppressing microlensing in the lens galaxy *and* scintillation caused by the Galactic ionized ISM. Situation 2: Only microlensing in the bulge/disk and halo in the lens galaxy occurs. Subsequent scatter-broadening in our galaxy does not suppress microlensing variability.

modulation indices of both images. No consistent solutions are found for an average mass of compact objects in the halo <1 $M_\odot$ for the range of MFs that we investigated. If we furthermore put a conservative upper limit of $\lesssim$0.5 $M_\odot$ on the average mass of compact objects in the bulge/disk of B1600+434 – which lies around the break in the Galactic bulge MF (e.g. Holtzman et al. 1998) – only MFs BS1–3 and BP1–4 (Table 2) remain viable MFs for the bulge/disk of B1600+434.

Constraints on $\Delta\theta$, f and $\mathcal{D}$: Using the MFs assumed viable above, we find from Table 3: $0.05\lesssim f\lesssim 0.11$ and $1.1\lesssim\mathcal{D}\lesssim 4.0$. Using Eq. (25) and the values of f and $\mathcal{D}$ listed in Table 3, the jet-component size then lies between $2\lesssim\Delta\theta_{\rm knot}\lesssim 5$ μas.

Constraints on $\beta_{\rm app}$: To estimate a time scale for strong microlensing variability, we calculate the average power spectrum

Table 4. The typical angular scale ($\theta_{\rm t}$) in μas between strong microlensing events in the simulated light curves, as defined through the power spectrum (see text). Listed are the values for two source sizes, 2 and 4 μas, approximately corresponding to the range of jet-component sizes that reproduce the observed modulation-index in the light curves (see text).

MF	$\Delta\theta_{\rm knot}$=2 μas	4 μas
AS6	8	14
AS7	8	13
AS8	10	14
AS9	13	14
BS1	7	13
BS2	7	12
BS3	7	12
BS4	8	14
BS5	10	14
BS6	8	15
BS7	8	18
BP1	7	14
BP2	6	12
BP3	7	16
BP4	7	12

of the 100 light curves for each MF, for the source size of 2 and 4 μas. The power-spectrum is typically relatively flat at low frequencies, smearing out the long-period modes in the light–curves. At higher frequencies the power drops rapidly. We therefore expect the strongest Fourier modes in the light curves to lie around the turn-over frequency, where the power drops to about 50%. Consequently, we define the typical angular scale of variability ($\theta_{\rm t}$) to correspond with the half-power frequency in the power-spectrum. In Table 4, we listed the results for those MFs that give a consistent solution (Table 3).

If we now take a separation of $\sim$2 weeks as indicative for the separation of strong modulations in light curve of image A (see days 80–140 in Figs. 1–2), we find an angular velocity of the jet-component in the source plane between 3 and 9 μas/week. Using Eq. (30), we then derive $9\lesssim\beta_{\rm app}\lesssim 26$. This range strongly depends on the local structure of the magnification pattern, which can differ strongly from place to place (e.g. Wambsganss 1990).

Constraints on $\beta_{\rm bulk}$ and ψ: Using the constraints of the Doppler factor ($\mathcal{D}$) and angular velocity of the jet-component ($\beta_{\rm app}$), one also obtains constraints on the angle between the jet–component direction with respect to the line-of-sight to the observer and the bulk velocity of the jet-component ($\beta_{\rm bulk}$). From Fig. 9, we subsequently find: $4^\circ\lesssim\psi\lesssim 13^\circ$ and $\beta_{\rm bulk}\gtrsim 0.995$, for the allowed ranges of these parameters.

Thus, several combinations of MFs for images A and B (Table 3) give solutions that reproduce the observed modulation-indices of both images for a consistent, although not unique, set of jet-component parameters. The derived constraints on the jet-component, however, do agree with observations of confirmed superluminal sources (e.g. Vermeulen & Cohen 1994).

5.3.2. Microlensing by compact halo objects

It appears we have found a lower limit of $\sim$1 $M_\odot$ on the mass of compact objects in the halo around the lens galaxy, under the assumptions that all variability we see is due to microlensing, the jet is dominated by a single component and there is no scatter-broadening. Let us now explore the implications of this in more detail, first mentioning several potential problems.

– Could microlensing be due to a globular cluster (GC) in the halo of the lens galaxy? It is easy to show that the probability of seeing a lensed image through a GC surface density $>$ $\kappa_{\rm GC}$ is

$$P(>\kappa_{\rm GC}) \approx \frac{N}{4\cdot\kappa_{\rm GC}^2}\left(\frac{\sigma_{\rm GC}}{\sigma_{\rm LG}}\right)^4. \quad (35)$$

We take a population of $N\sim$150 GCs inside the Einstein radius of the lens galaxy (LG), with a velocity dispersion of $\sigma_{\rm GC}$=7 km s^{-1}. These values are typical of those found for our galaxy (e.g. Binney & Merrifield 1999). Using $\sigma_{\rm LG}\approx$200 km s^{-1} (KBJ98), $\kappa_{\rm GC}=\kappa_{\rm A}$=0.2, we then find a probability $P(>\kappa_{\rm GC})\approx 1.7\cdot10^{-3}$ that the microlensing optical depth ($\tau_{\rm ml}\approx\kappa_{\rm ml}$) of the GC exceeds that of the dark matter halo. The probability that $\kappa_{\rm GC}$ exceeds $\kappa_{\rm B}$=0.9, thereby causing similar or larger microlensing variability, is $7\cdot10^{-5}$. Hence, it is very unlikely that a GC in the line-of-sight to lensed image A could enhance the microlensing optical depth significantly.

– What is the influence of binary systems on the mass limit of a compact object in the dark matter halo? We know that a large fraction of stars in the bulge is locked up in binary systems (e.g Holtzman et al. 1998). In the case of high microlensing optical depths, one can consider a binary as a single microlensing object, with a mass equal to the sum of the individual masses.
From Table 2 we see that a higher mass of compact objects gives a higher microlensing modulation-index for a given source size. Hence, if we know the typical stellar mass of objects in the bulge/disk and assume they are all single objects, not in a binary system, we underestimate its modulation-index. One has to take this effect into account.

Having dealt with these possible complications, let us explore the lower mass limit of the compact objects in more detail. If we assume that (i) all compact object in the bulge/disk are not in binary systems and (ii) all compact objects are in binary systems and (iii) use the lowest average mass of objects in the bulge/disk (Tables 2–3), we find a very conservative lower limit of 0.5 $M_\odot$ on the mass of individual compact objects in the halo. In the more realistic case where most of the stars in the bulge/disk are in binaries and most compact objects are probably not, a lower limit of 1.5 $M_\odot$ is found, assuming that the average bulge/disk stellar mass in the halo is $\sim$0.1 $M_\odot$. If the bulge/disk stars have average masses somewhere between 0.1 and 0.3 $M_\odot$ and are foremost in binaries, the lower limit increases to $\sim$2.5 $M_\odot$.

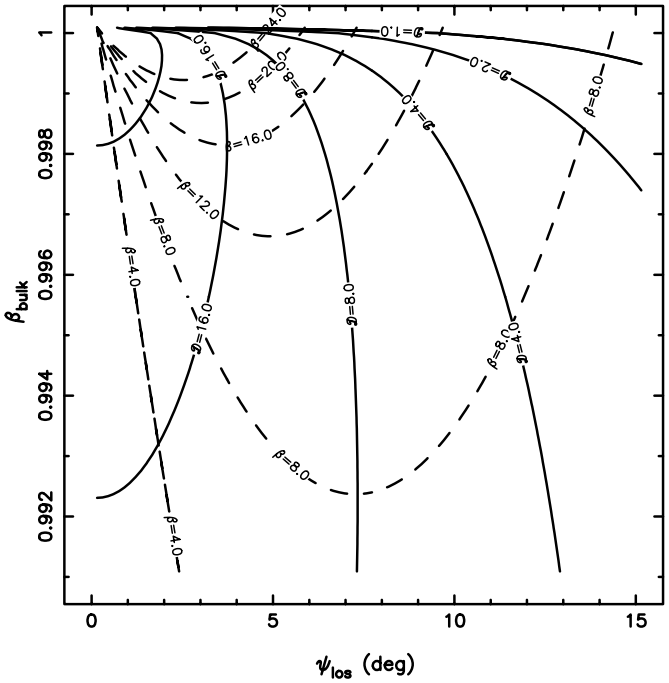

Fig. 9. The bulk velocity ($\beta_{\rm bulk}$) and angle with respect to the the line-of-sight to the observer (ψ) of a relativistic jet-component, as a function of its Doppler boosting ($\mathcal{D}$) and apparent velocity ($\beta_{\rm app}$), calculated using Eqs. (20) and (26).

Table 5. Summary of constraints on the jet-component parameters, derived within the context of the microlensing hypothesis. We assume $T_{12}^{\rm b,ic}$=0.5 and a flat FRW universe with $\Omega_{\rm m}$=1 and H_0=65 km s^{-1} Mpc^{-1}.

Fraction flux	$0.05 \lesssim f \lesssim 0.11$	
Doppler factor	$1.1 \lesssim \mathcal{D} \lesssim 4.0$	
Size in source plane	$2 \lesssim \Delta\theta_{\rm knot} \lesssim 5$	(μas)
Apparent velocity	$9 \lesssim \beta_{\rm app} \lesssim 26$	
LOS angle of jet	$4 \lesssim \psi_{los} \lesssim 13$	($^\circ$)
Bulk velocity	$\beta_{\rm bulk} \gtrsim 0.995$	

As in the case of scintillation, scatter-broadening of image B also suppresses microlensing (Sect. 5.3). If this happens, one would underestimate the true microlensing modulation-index of image B. This would give one more freedom to decrease f and/or increase $\mathcal{D}$ for the microlensed jet-component, thereby changing the required average mass of compact objects in the halo. It would, however, *never* eliminate the need for them.

6. Microlensing of a realistic jet structure

So far, we have only investigated a very simple model of the source structure, consisting of a core plus a single jet-component. To see how a real source behaves, when microlensed by similar MFs as in the lens galaxy of B1600+434, we simulated light curves of a more complex jet structure.

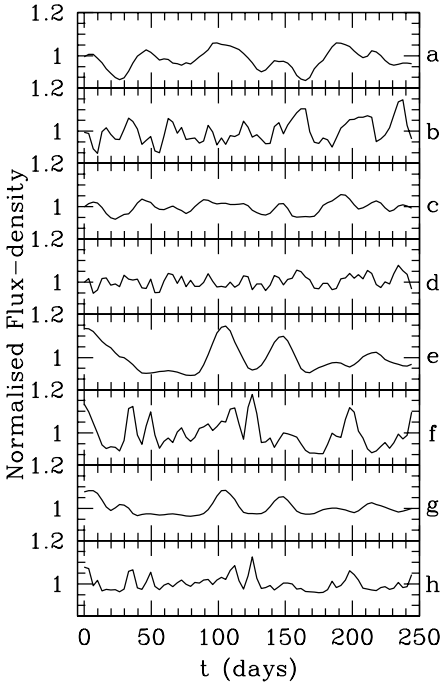

Fig. 10. Eight simulated microlensing light curves of 3C120. The parameters for each light curve are listed in Table 6.

6.1. The jet structure of 3C120

We used the inner jet-structure seen in 3C120 (Gómez et al. 1998; Gómez, Marscher & Alberdi 1999) as a 'template', because it is one of the best-studied nearby jet structures. The inner jet consists of a core plus at least 15 distinguishable jet-components (Gómez et al. 1999), which move superluminally, with velocities typically around $4.5c$ (H_0=65 km s^{-1} Mpc^{-1}; Gómez et al. 1998). The jet was observed at 22 GHz. The total flux density of 3C120 at this frequency is 5.7±0.9 Jy (O'Dell et al. 1978), whereas the fitted inner-jet components contain about 2.5 Jy (Gómez et al. 1999). We therefore assume that the inner jet contains about 40% of the total flux density of 3C120.

Note that 22 GHz corresponds to approximately X–band (8.5 GHz) observations, when placed at the source redshift of B1600+434 (z=1.59). We thus scale the size of the jet structure down by the ratio of angular diameters distances for 3C120 and the lensed source of B1600+434 and its flux density by the ratio of luminosity distances squared.

At a redshift of z=1.59, 3C120 would be a 1.8 mJy source. To obtain a source of about 25 mJy total, as observed for B1600+434, we scale each jet component's size by a factor $\alpha_{\rm r}$=3.7 in radius and assume that about 60% of its flux density is contained in an extended structure, which is not sensitive to microlensing. We assume their surface brightness temperature to be conserved and associate the radius of the source with half the FWHM of the component size determined by Gómez et al. (1999). The resulting jet structure has a flux density of about 25 mJy at 8.5 GHz and an angular size of the inner jet less than 1 mas. If we only use the inner jet and not assume the additional 60% of extended emission, one should scale the inner-jet-components by a factor of $\alpha_{\rm r}$=5.7 to obtain a total flux density of about 25 mJy.

Table 6. Scaling parameters for 3C120 and results from eight arbitrary simulated light curves. LCs $a-d$ show light curves using the MF B2, whereas LCs $e-h$ show light curves using the MF A7.

LC	$\alpha_{\rm r}$	$\alpha_{\rm v}$	rms (%)	$t_{\rm typ}$ (d)
a	5.7	1	4.5	∼50
b	5.7	3	5.4	∼15
c	3.7	1	2.6	∼35
d	3.7	3	2.9	∼10
e	5.7	1	6.4	∼50
f	5.7	3	6.7	∼20
g	3.7	1	3.3	∼40
h	3.7	3	3.4	∼15

6.2. Microlensed light curves of 3C120

The jet structure is randomly placed on the magnification pattern. We recalculate the jet structure and the resulting normalized light curves at epochs separated by 3.3 days, which is the average sampling of the light curves of B1600+434. For image A, we use the MF AS7, which corresponds to a halo filled with stellar remnants, such as black holes and neutron stars. For image B, we use the MF BS2.

We calculate light curves with a total time span of 35 weeks, corresponding to the length of the observed VLA light curves of B1600+434. We subsequently scale the light curves by a factor 0.4 ($\alpha_{\rm r}$=3.7 for 40% of the flux density from the inner jet) or 1.0 ($\alpha_{\rm r}$=5.7 for 100% of the flux density from the inner-jet). We repeat these simulations using an apparent velocity three times larger ($\alpha_{\rm v}$=3).

In Fig. 10, one simulated light curve is shown for the images A and B, for each size scale factor ($\alpha_{\rm r}$) and velocity scale factor ($\alpha_{\rm v}$). The modulation-index and estimated variability time scale between strong microlensing events are listed in Table 6.

6.3. A comparison with B1600+434

Not only does the modulation-index correspond well with that seen for B1600+434–A and B, also the time scale of variability is in the order of several weeks to months (depending on the choice of $\alpha_{\rm v}$; Table 6). The similarity between some of the simulated light curves and those observed for B1600+434 is remarkable, knowing that we have not resorted to extreme assumptions.

We therefore regard these simulations as 'proof of principle', showing that microlensing of multiply-imaged compact flat-spectrum radio sources, of which more and more are being discovered – for example in the CLASS/JVAS survey (e.g Browne et al. 1998) – can be a very common occurrence, enabling us to study both the structure of these high–z radio sources, as well as the MF of compact objects in the intermediate–z lens galaxies.

7. Microlensing versus scintillation

We have seen many arguments in Sects. 3–5, for and/or against scintillation and microlensing as the cause of variability in compact flat-spectrum radio sources. Both can in principle explain the observed modulation-index and variability time scales in the VLA 8.5–GHz light curves in the individual lensed images of B1600+434, although it remains very difficult to explain the longer ($\gg$1 day) variations in the light curves or the difference in modulation-index between the two lensed images in terms of scattering. In the case of microlensing, one would expect to see scintillation at some level as well, possibly complicating a straightforward analysis. How can we then separate these mechanisms as the dominant cause of variability?

Scintillation and microlensing have different dependencies on frequency. Although microlensing is achromatic, the frequency dependence of the source structure predicts a clear dependence of the microlensing variability as a function of frequency. For flat-spectrum synchrotron self-absorbed source sources, the source size is inverse proportional to frequency (Eq. (24)). Thus the modulation-index decreases with decreasing frequency (Eq. (32)). In the case of weak and strong refractive scattering (i.e. flickering), however, the modulation-index usually increases with decreasing frequency (e.g. BNR86; Narayan 1992; Rickett et al. 1995). *The key to testing whether the observed short-term variability in gravitationally lensed flat-spectrum radio sources is partly or fully dominated by microlensing or scintillation is therefore their strong opposite dependence on frequency.*

In Fig. 11, we have plotted the dependence of the modulation index in the case of weak and strong refractive scintillation versus that of microlensing. We assume that the source or jet-component size scales as ν^{-1} and that scatter-broadening is negligible. All curves are normalized at $m_{\rm part}$=3.7% at 6 cm, as measured with the WSRT in 1999 (Table 1). We determine the modulation-index from scintillation following Rickett et al. (1995) and that from microlensing using Eq. (32). In the case of microlensing, we use the maximum range of the turn-over scale $\Delta\theta_{\rm b}$=0.9–4.5 μas and the jet-component size at 8.5 GHz $\Delta\theta_{\rm knot}$=2–5 μas, found from Tables 2 and 5. We furthermore assume that the short-term variability is dominated by image A, as observed in the VLA 8.5–GHz light curves. The resulting curves show a clear opposite trend as a function of wavelength and therefore act as a strong discriminator between microlensing and scintillation. The constraints on the microlensing curves were determined from the VLA 8.5–GHz light curves only and therefore independent from the WSRT 1.4 and 5–GHz modulation-indices.

From the WSRT modulation-indices ($m_{\rm part}$) at 1.4 and 5 GHz (Table 1), one finds $m_{21}/m_6\approx$0.31, as indicated by the open circle in Fig. 11. Although this result is based on two frequencies only, it clearly agrees much better with the predictions from microlensing and not that from scintillation! The latter would require a $\sim$8 times larger value for m_{21} (i.e about 9%). We do not plot the VLA 8.5–GHz modulation-index, because it was determined from a different epoch. The modulation-index

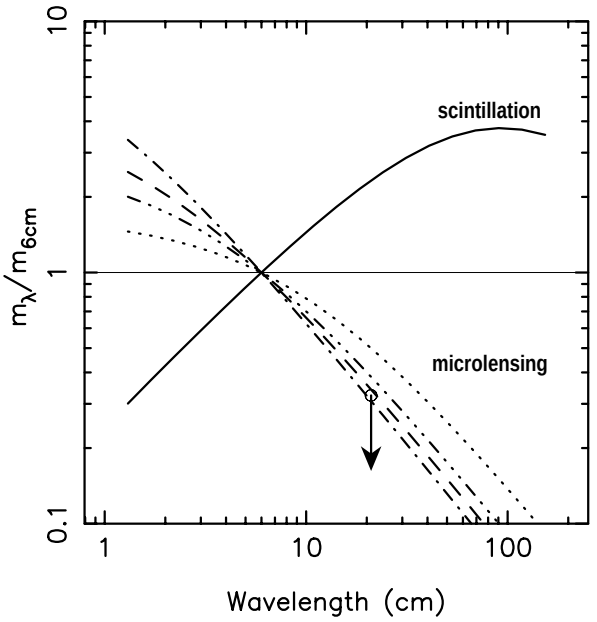

Fig. 11. Dependence of the modulation-index from scintillation and microlensing on wavelength. The solid line shows the modulation-index from scintillation. The dashed and dot-dashed lines show the modulation-indices from microlensing, using $\Delta\theta_{\rm knot}$=2 and 5 μas at 8.5 GHz, respectively, assuming $\Delta\theta_{\rm b}$=0.9 μas. The dotted and dash-dot-dotted lines indicates the same for $\Delta\theta_{\rm b}$=4.5 μas. All curves are normalized to the $m_{\rm part}$=3.7% modulation at 6.0 cm observed with the WSRT in 1999 (Table 1). The open circle indicates the upper limit on the ratio m_{21}/m_6 (Table 1).

from microlensing and scintillation might change as function of time, whereas the ratio of modulation-indices, measured simultaneously, is less likely to change.

Thus, if all short-term variability seen in the light curves of B1600+434 is external, it follows the predictions from microlensing. Moreover, if the short-term variability seen in the WSRT 1.4 and 5–GHz light curves is intrinsic, this would be very hard to reconcile with the fact that in 1998 almost all of the VLA 8.5–GHz short-term variability was shown (see Sect. 2) to be external. The most logical conclusion from all this is that the short-term variability at 1.4, 5 and 8.5 GHz is dominated by microlensing. This explains both the modulation-indices as function of frequency at 1.4 and 5 GHz and the longer variability time scale in the VLA 8.5–GHz light curves. In the case of scintillation, one would require either different sizes of the lensed images or a very different ionized ISM towards the images and also a different time scale and frequency-dependence of scattering from that expected from a Kolmogorov spectrum of inhomogeneities of the ionized ISM. All evidence thus far is therefore *only* consistent with microlensing as the dominant cause of the observed short-term variability.

8. Summary and conclusions

We have shown *unambiguous* evidence of external variability in the CLASS gravitational lens B1600+434. The difference

between the 8.5–GHz VLA light curves of the two lensed images shows external variability at the 14.6–σ confidence level. The modulation indices of the short-term variability are 2.8% for image A and 1.6% for image B. The difference light curve has an rms scatter of 2.8%, indicating that the short-term variability in both light curves is mostly of external origin (Sect. 2).

We have investigated two plausible sources of this external variability: (i) scattering by the ionized component of the Galactic interstellar medium (ISM) and (ii) microlensing by massive compact objects in the bulge/disk and halo of the lens galaxy.

Based on the 'standard' theory of scintillation (e.g. Narayan 1992; Rickett et al. 1995) there should be a considerable increase in the modulation-index with wavelength (Sects. 3 and 7). From simultaneous WSRT 1.4 and 5–GHz observations we find, however, that m_{21}=1.2% and m_6=3.7% (Table 1), which is a considerable decrease. Scintillation theory predicts m_{21}=9.0% for m_6=3.7% (Sect. 7). If the 1.4 and 5–GHz short-term variability is intrinsic, it is hard to reconcile with the fact that in 1998 the VLA 8.5–GHz light curves were dominated by external variability during the full eight months of monitoring (Sect. 2), although it can not be fully excluded yet. Moreover, from microlensing simulations, we expect that m_{21}=1.2–2.4% if $m_6 = 3.7\%$ (Fig. 11), based on constraints on the source structure and mass function of compact objects found from the VLA 8.5–GHz light curves (Sects. 4, 5 and 7). This range agrees remarkably well with the observed modulation index $m_{\rm part}$=1.2% at 21 cm.

Supplementary to this argument, the difference in modulation-index between the lensed images would, in the case of scintillation, argue for either a very different Galactic ionized ISM ($\rm SM_A/SM_B \approx 3.1$; Sect. 3.1–2) towards the lensed images or a different image size ($\Delta\theta_{\rm B}/\Delta\theta_{\rm A} \approx 1.75$; Sect. 3.2), although the latter might result from scatter-broadening. Furthermore, the longer variability time scales at 8.5 GHz ($\gg$1 day; Figs. 1–2) are also difficult to explain in terms of scintillation, as well as the absence of variability with short time scales in several 12 h WSRT observations at 5 GHz (Koopmans et al. in prep.).

However, the strongest argument against scintillation remains the dominant presence of short-term external variability at 8.5 GHz in 1998, combined with the fact that in 1999 significant short-term variability is seen at 5 GHz, but almost none at 1.4 GHz.

Under the microlensing hypothesis, we find a consistent, although not unique set of jet-component parameters. A core plus a single-jet-component with a size of 2–5 μas, containing 5–11% of the flux density and moving superluminally with $9 \lesssim \beta_{\rm app} \lesssim 26$, can explain the modulation-index and variability time scale in both lensed images (Sects. 4–5). For image A we find a significantly higher average mass of compact objects ($\gtrsim$0.5 $\rm M_\odot$), compared with those near image B. A much lower mass of compact object would result in a finer magnification pattern and thus in less variability. If image B is scatter-broadened, its microlensing modulation-index is reduced, which might change the lower-limit on the compact object mass.

If one, based on the evidence gathered thus far, accepts that the 1.4, 5 and 8.5–GHz short-term variability in B1600+434–A and B is dominated by microlensing, the profound consequence is that the dark-matter halo at $\sim$6 kpc above the plane of the disk-galaxy lens in B1600+434 is partly filled with massive compact objects. New WSRT, VLA and VLBI multi-frequency data is being obtained at the moment, which combined with a more comprehensive statistical analysis should provide us with refined constraints on the mass function of compact objects and the source structure (Koopmans et al. in prep.).

Acknowledgements. The authors would especially like to thank Joachim Wambsganss for making available and giving support in using his microlensing code. They thank Frank Briggs for providing useful supermongo code, and Joachim Wambsganss, Jane Dennett-Thorpe, Penny Sackett, Jean-Pierre Macquart and Roger Blandford for useful discussions. They also thank the referee, Andreas Quirrenbach, for pointing out several important issues. LVEK and AGdeB acknowledge the support from an NWO program subsidy (grant number 781-76-101). This research was supported in part by the European Commission, TMR Programme, Research Network Contract ERBFMRXCT96-0034 'CERES'. The National Radio Astronomy Observatory is a facility of the National Science Foundation operated under cooperative agreement by Associated Universities, Inc. The National Radio Astronomy Observatory is a facility of the National Science Foundation operated under cooperative agreement by Associated Universities, Inc. The Westerbork Synthesis Radio Telescope (WSRT) is operated by the Netherlands Foundation for Research in Astronomy (ASTRON) with the financial support from the Netherlands Organization for Scientific Research (NWO).

References

Becker R.H., White R.L., Edwards A.L., 1991, ApJS 75, 1
Biggs A.D., Browne I.W.A., Helbig P., et al., 1999, MNRAS 304, 349
Blandford R.D., Königl A., 1979, ApJ 232, 34
Blandford R., Narayan R., Romani R.W., 1986, ApJL 301, L53 [BNR86]
Browne I.W.A., 1998, In: Bremer M., Jackson N.J. (eds.) Observational Cosmology with the New Radio Surveys, p. 323
Chang K., Refsdal S., 1979, Nature 282, 561
Chu L.B., Baath F.T., Rantakyroe F.J., Zhang H.S., Nicholson G., 1996, A&A 307, 15
Condon J.J., Ledden J.E., O'Dell S.L., Dennison B., 1979, AJ 84, 1
Cordes J.M., Weisberg J.M., Boriakoff V., 1985, ApJ 288, 221
Corrigan R.T., Irwin M.J., Arnaud J., et al., 1991, AJ 102, 34
Deguchi S., Watson W.D., 1987, Physical Review Letters, 59, 2814
Dennett-Thorpe J., de Bruyn A.G., 2000, ApJL 529, L65
Fassnacht C.D., Cohen J.G., 1998, AJ 115, 377
Fassnacht C.D., Pearson T.J., Readhead A.C.S., et al., 1999, ApJ accepted
Gomez J.-L., Marscher A.P., Alberdi A., Marti J. M., Ibanez J.M., 1998, ApJ 499, 221
Gómez J.-L., Marscher A.P., Alberdi A., 1999, ApJL 521, L29
Gopal-Krishna, Subramanian K., 1991, Nature 349, 766
Haarsma D.B., Hewitt J.N., Lehár J., Burke B.F., 1997, ApJ 479, 102
Heeschen D., 1982, IAU Symposia, 97, 327
Heeschen D.S., 1984, AJ 89, 1111
Holtzman J.A., Watson A.M., Baum W.A., 1998, AJ 115, 1946
Irwin M.J., Hewett P.C., Corrigan R.T., Jedrzejewski R.I., Webster R.L., 1989, AJ 98, 1989

Jackson N., de Bruyn A.G., Myers S., et al., 1995, MNRAS 274, L25
Jaunsen A.O., Hjorth J., 1997, A&A 317, L39
Kellermann K.I., Pauliny-Toth I.I.K., 1969, ApJL 155, L71
Koopmans L.V.E., De Bruyn A.G., Jackson N., 1998, MNRAS 295, 534 [KBJ98]
Koopmans L.V.E., De Bruyn A.G., Xanthopoulos E., Fassnacht C.D., 2000, A&A 356, 391 [KBXF00]
Kormann R., Schneider P., Bartelmann M., 1994, A&A 284, 285
Kraus A., Quirrenbach A., Lobanov A.P., et al., 1999, A&A 344, 807
Kundić T., et al., 1997, ApJ 482, 75
Lehár J., Hewitt J.N., Burke B.F., Roberts D.H., 1992, ApJ 384, 453
Lewis G.F., Williams L.L.R., 1997, MNRAS 287, 155
Lewis G.F., Irwin M.J., Hewett P.C., Foltz C.B., 1998, MNRAS 295, 573
Lovell J.E.J., Jauncey D.L., Reynolds J.E., et al., 1998, ApJ 508, L51
Maller A.H., Simard L., Guhathakurta P., et al., 2000, ApJ 533, 194
Miller G.E., Scalo J.M., 1979, ApJS 41, 513
Munoz J.A., Falco E.E., Kochanek C.S., et al., 1999, AP&SS 263, 51
Narayan R., 1992, Phil. Trans. Roy. Soc., 341, 151
O'Dell S.L., Puschell J.J., Stein W.A., et al., 1978, ApJ 224, 22
Ostensen R., Refsdal S., Stabell R., et al., 1996, A&A 309, 59
Patnaik A.R., Menten K.M, Porcas R.W., Kemball A.J., 1999, in preparation
Pelt J., Kayser R., Refsdal S., Schramm T., 1996, A&A 305, 97
Quirrenbach A., Witzel A., Krichbaum T., Hummel C.A., Alberdi A., 1989, Nature 337, 442
Quirrenbach A., Kraus A., Lobanov A., et al. 1998, American Astronomical Society Meeting, 192, 3603
Refsdal S., 1964, MNRAS 128, 295
Refsdal S., Stabell R., 1991, A&A 250, 62
Refsdal S., Stabell R., 1997, A&A 325, 877
Rengelink R.B., Tang Y., De Bruyn A.G., et al., 1997, A&ASS 124, 259
Rickett B.J., 1977, ARA&A 15, 479
Rickett B.J., 1990, ARA&A 28, 561
Rickett B.J., Coles W.A., Bourgois G., 1984, A&A 134, 390
Rickett A., Quirrenbach B.J., Wegner R., Krichbaum T.P., Witzel A., 1995, A&A 293, 479
Romero G.E., Surpi G., Vucetich H., 1995, A&A 301, 641
Salpeter E.E., 1955, ApJ 121, 161
Schechter P.L., Bailyn C.D., Barr R., et al., 1997, ApJL 475, L85
Schneider P., Ehlers J., Falco E.E., 1992, Gravitational Lenses, Springer-Verlag Berlin Heidelberg New York.
Schmidt R., Wambsganss J., 1998, A&A 335, 379
Schramm K.-J., Borgeest U., Camenzind M., et al., 1993, A&A 278, 391
Simonetti J.H., Cordes J.M., Heeschen D.S., 1985, ApJ 296, 46
Stickel M., Fried J.W., Kuehr H., 1988, A&A 198, L13
Takalo L.O., Sillanpaeae A., Valtaoja E., et al., 1998, A&ASS 129, 577
Taylor J.H., Cordes J.M., 1993, ApJ 411, 674
Timmes F.X., Woosley S.E., Weaver T.A., 1996, ApJ 457, 834
Vermeulen R.C., Cohen M.H., 1994, ApJ 430, 467
Wagner S.J., Witzel A., 1995, ARA&A 33, 163
Wagner S.J., Witzel A., Heidt J., et al., 1996, AJ 111, 2187
Walker M.A., 1998, MNRAS 294, 307 [W98]
Wambsganss J., 1990, Thesis Ludwig-Maximilians-Univ., Munich (Germany, F.R.). Fakultät für Physik.
Wambsganss J., 1999, Journ. of Comp. and Appl. Math. 109, 353
Watson D., Hanlon L., McBreen B., et al. 1999, A&A 345, 414
Woźniak, P. R., Alard, C., Udalski, A., et al., 2000, ApJ 529, 88
Wyithe, J. S. B., Webster, R. L. & Turner, E. L. 1999, MNRAS 309, 261